

# Night-Voyager: Consistent and Efficient Nocturnal Vision-Aided State Estimation in Object Maps

Tianxiao Gao\*, Mingle Zhao\*, Chengzhong Xu, and Hui Kong

**Abstract**—Accurate and robust state estimation at nighttime is essential for autonomous robotic navigation to achieve nocturnal or round-the-clock tasks. An intuitive question arises: Can low-cost standard cameras be exploited for nocturnal state estimation? Regrettably, most existing visual methods may fail under adverse illumination conditions, even with active lighting or image enhancement. A pivotal insight, however, is that streetlights in most urban scenarios act as stable and salient prior visual cues at night, reminiscent of stars in deep space aiding spacecraft voyage in interstellar navigation. Inspired by this, we propose Night-Voyager, an object-level nocturnal vision-aided state estimation framework that leverages prior object maps and keypoints for versatile localization. We also find that the primary limitation of conventional visual methods under poor lighting conditions stems from the reliance on pixel-level metrics. In contrast, metric-agnostic, non-pixel-level object detection serves as a bridge between pixel-level and object-level spaces, enabling effective propagation and utilization of object map information within the system. Night-Voyager begins with a fast initialization to solve the global localization problem. By employing an effective two-stage cross-modal data association, the system delivers globally consistent state updates using map-based observations. To address the challenge of significant uncertainties in visual observations at night, a novel matrix Lie group formulation and a feature-decoupled multi-state invariant filter are introduced, ensuring consistent and efficient estimation. Through comprehensive experiments in both simulation and diverse real-world scenarios (spanning approximately 12.3 km), Night-Voyager showcases its efficacy, robustness, and efficiency, filling a critical gap in nocturnal vision-aided state estimation.

**Index Terms**—Localization, SLAM, Sensor Fusion, State Estimation, Object Map

## I. INTRODUCTION

**D**RIVEN by significant advancements in robotics and automation, mobile robots are experiencing widespread adoption in industrial applications, including transportation, logistics, and search-and-rescue operations [1]. Among all the essential capabilities, all-time, all-weather autonomous navigation is a fundamental manifestation of robotic autonomy. However, achieving highly resilient localization in low-illumination nocturnal scenarios during navigation typically requires the deployment of high-cost and specialized sensors, such as Light Detection And Ranging (LiDAR) sensors, infrared cameras, high-precision Global Navigation Satellite Systems (GNSS), and Inertial Navigation Systems (INS). In contrast, standard cameras have the advantages of portability, low cost, and informative measurements. However, utilizing standard cameras for robot localization and navigation in nighttime environments

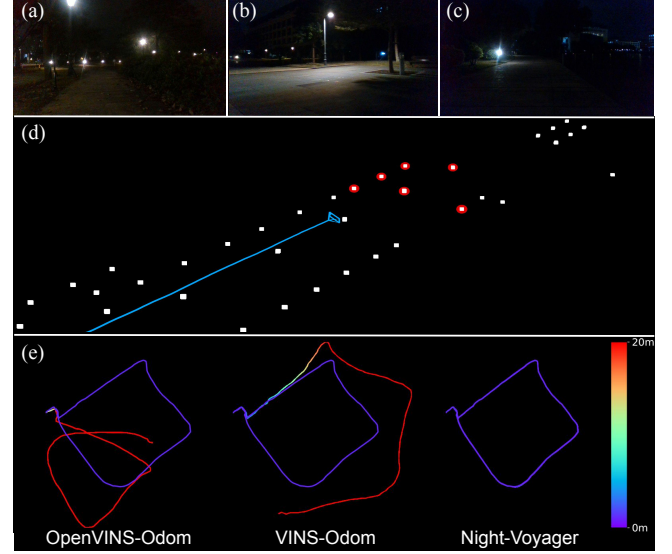


Fig. 1: Comparison of different vision-aided state estimation methods. (a), (b), and (c) are camera images captured in nocturnal scenes. (d) displays the online localization (the blue curve) of Night-Voyager within the streetlight map (white boxes) and the matches (red spheres) via the proposed data association approach. (e) depicts the trajectories estimated by the odometer-aided OpenVINS [2] (OpenVINS-Odom), the odometer-aided VINS-Mono [3], [4] (VINS-Odom), and Night-Voyager, respectively. The color bar indicates the trajectory error scale with respect to the ground truth (purple curves).

seems highly counterintuitive, and notably, the key challenge lies in the nocturnal visual state estimation.

### A. Nocturnal Visual State Estimation

Therefore, a natural question arises: Is it feasible to achieve accurate and robust state estimation in low-illumination nocturnal environments using low-cost, standard camera-centric sensors with generic parameters, which are primarily designed for well-illuminated conditions? Unfortunately, conventional vision-aided state estimation or Simultaneous Localization And Mapping (SLAM) methods [2]–[9] are prone to failures, as shown in Fig. 1. This is attributed to the fact that unfavorable, unstable, and inconsistent illumination conditions could lead to insufficient or erroneous data association. Besides, the limited visual information available in dark scenes can increase pose drifts, potentially resulting in system failures. Intuitively, a practical solution is to install active heading lights on robots. However, as shown in Fig. 2, the empirical evidence suggests a reality that is contrary to initial expectations. On the one hand, active lighting and dynamic motions can exacerbate the inconsistent, imbalanced, and radical illumination variance,

thereby increasing the challenge of data association [10]–[12]. On the other hand, illuminated and enhanced airborne particles and dust [13], [14], as well as high-reflectivity objects [11], are sparkling in camera images owing to backscatter [15]. This phenomenon could affect the feature tracking, leading to deteriorated and chaotic data association results. To solve these issues from active lighting, sophisticated camera lens design or low-illumination environment-specific parameter tuning in Image Signal Processing (ISP) algorithms or camera control functions is necessary in different environments [16]–[18]. Consequently, although the active lighting solution is direct and aligns with common intuition, it fails to fundamentally address the underlying problem of nocturnal visual state estimation in low-illumination environments.

### B. Bottleneck and Crux

The underlying problem of nocturnal visual state estimation stems from two primary bottleneck factors: *insufficiency* and *inconsistency*. First, the insufficiency indicates the lack of prominent visual features in dark nocturnal environments, which prevents the system from leveraging effective and accurate observations to update states in time. Second, even when prominent visual features are present (e.g., from active lighting or locally illuminated areas), these features are often inconsistent, transient, and typically originate from dynamic objects (e.g., illuminated dust particles). To alleviate the *insufficiency* issue in low-illumination environments, researchers explore numerous classical image processing methods [19]–[21] and deep learning-based methods [22]–[27] to enhance low-light images. Nevertheless, the generalization and real-time performance of these methods fail to meet the requirements of robotic applications, rendering them challenging to be deployed on robotic platforms. Crucially, these methods are unable to maintain temporal photometric consistency between images, which consequently impacts the performance of data association and exaggerates the *inconsistency* issue. In parallel, extensive works are proposed to achieve robust and consistent image feature matching [28]–[37]. However, these methods are also found to be challenging to apply in low-illumination images and dark environments [38], [39]. Furthermore, the issues of generalization, parameter tuning, and real-time performance also represent bottlenecks for online robotic applications.

Significantly, the two key bottleneck factors in nocturnal visual state estimation highlighted above – namely, *insufficiency* and *inconsistency* – point to a common crux and a fundamental insight: current conventional visual methods heavily rely on *pixel-level* visual features and *pixel-level* data association approaches. Therefore, relying solely on the *pixel-level* feature and data association is not an essentially seminal and ultimate solution for nocturnal visual state estimation. As for tackling the issues of *insufficiency* and *inconsistency*, is there a solution that can provide salient visual features in nighttime environments, while ensuring these features remain consistent, stable, and non-pixel-level? This represents an essential problem in nocturnal visual state estimation. Inspired by the stellar-inertial navigation of spacecraft in deep space (e.g., the Voyager Mission) [40]–[43] or the human celestial navigation in the wilderness [44], which exploits priori

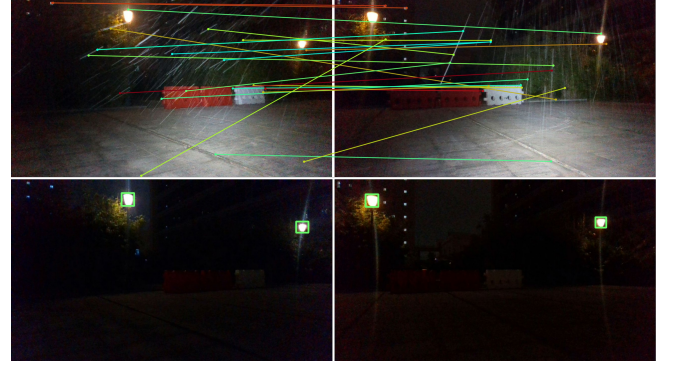


Fig. 2: Top row: active lighting can further aggravate inconsistent and imbalanced illumination issues while amplifying the backscatter effect caused by sparkling particles, resulting in a significant number of erroneous feature matches (colored dots and lines). Bottom row: object-level detection remains extraordinarily robust to varying lighting conditions. Even in low-light or completely dark nighttime scenarios, streetlights can consistently serve as stable and salient object-level features for detection (green detection boxes).

ephemeris data and star coordinates to achieve localization, we realize that utilizing the priori environmental map information represents a fundamental and effective avenue for addressing the aforementioned challenges in nocturnal scenes. Fortunately, for low-illumination nocturnal environments, an important discernment is that sufficient static streetlights can provide a stable source of rare object-level perceptive information in most urban scenarios (e.g., nighttime campuses, parks, factories, or streets). Additionally, the light saturation makes streetlights easily detectable from images, crucially at the object level instead of the pixel level. Consequently, these insights motivate us to explore priori lightweight streetlight maps and object-level association methods to achieve globally consistent and drift-bounded nocturnal visual state estimation.

### C. Proposed Methodology and Framework

Despite the benefits of object-level streetlight detection, there are several challenges in leveraging it to achieve generic visual state estimation. First, due to the high similarity between different streetlight detections in images, designing discriminating descriptors for streetlight data association or feature maps is not feasible. Hence, the localization based on conventional visual-feature correspondences or visual maps is unreliable and error-prone. Second, the substantial uncertainties inherent in nighttime visual observations coupled with the considerable errors in initialization compel us to design a robust, consistent, and efficient state estimator in theory. Third, a fast and accurate initialization module, which is essentially dominated by a global localization problem within the prior map, is indispensable for the convergence of online state estimator. In addition, owing to the intrinsic sparsity of streetlights, degenerate and tracking lost cases are inevitable when few streetlights are visible within the camera’s Field of View (FoV). Accordingly, pose estimates are susceptible to rapid drifts in the absence of global constraints.

To address these issues, this work introduces Night-Voyager, a hybrid object-level and pixel-level state estimation framework, achieving robust and versatile nocturnal vision-aided

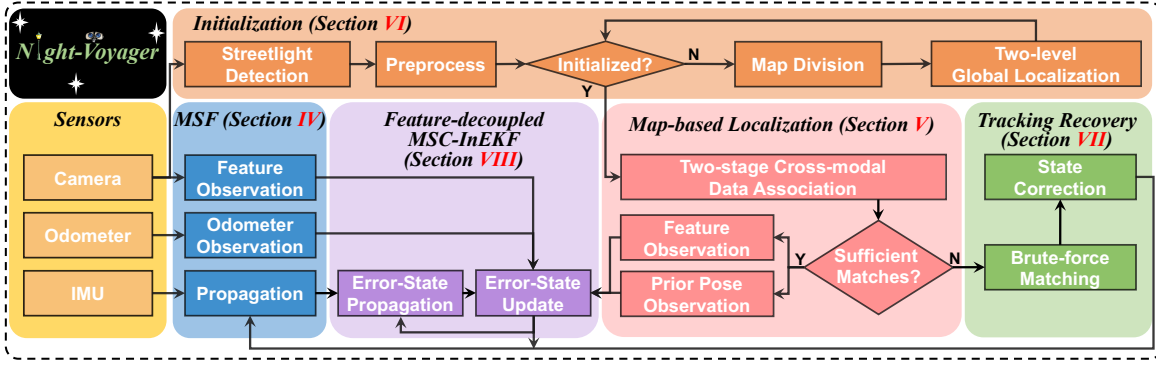


Fig. 3: System overview of the proposed consistent and efficient nocturnal vision-aided state estimation framework, Night-Voyager.

state estimation in object maps. The Night-Voyager framework is presented in Fig. 3. For nighttime cases, the reuse of collected LiDAR maps can be combined with object detection methods to generate extremely lightweight streetlight maps. Night-Voyager starts with the multi-sensor fusion module (MSF) (Section IV) and the initialization (Section VI) concurrently. The initialization is performed in a divide-and-conquer scheme, thereby dividing the map-based global localization problem into a series of *Perspective-Three-Point* (P3P) problems [45]. A two-stage cross-modal data association approach further ensures the accuracy and robustness of the detection-map matching process, providing reliable observations for state update (Section V). Besides, the MSF module that fuses keypoints with other sensor measurements is independent of other modules. This design enables the system to achieve accurate state estimation in both dark nighttime and well-illuminated scenarios. Thus, Night-Voyager actually constitutes a complete and all-day vision-aided state estimation framework. More importantly, with a novel matrix Lie group formulation, a feature-decoupled Multi-State-Constraint Invariant Extended Kalman Filter (MSC-InEKF) is designed (Section VIII), endowing Night-Voyager with a consistent and efficient state estimator that attains the significantly accurate localization at night. The designed matrix Lie group-based filter can ensure stability, convergence, and consistency in state estimation, making it particularly robust for nocturnal state estimation, even in scenarios characterized by high observation noise, prolonged absence of valid observations, and considerable initialization errors. When streetlight matches are absent for a while, the tracking recovery module (Section VII) is triggered to correct the state estimate. Extensive experiments on simulation, public sequences, and the collected dataset validate the effectiveness and performance of the proposed methodology. Compared with the previous work Night-Rider [46], Night-Voyager features novel advancements in:

- 1) A novel and efficient filter design. In contrast to Night-Rider only utilizing current observations, the multi-state-constraint and the feature-decoupled traits substantially enhance the estimation accuracy and efficiency.
- 2) A more robust cross-modal data association approach. The innovative error design improves the ability to identify correct matches and the adaptability to adjust the requirement for finding matches.
- 3) A versatile and generic framework architecture. Night-

Rider requires a manually specified initial pose and operates only at night. In comparison, the fast initialization and MSF enable Night-Voyager to perform autonomous state estimation throughout diverse all-day scenarios.

- 4) The usage of pixel-level features and prior poses for accuracy improvement and generality. In contrast, Night-Rider only utilizes streetlight detections for localization.
- 5) A precise modeling of streetlight observations. The virtual center of streetlight clusters significantly improves localization accuracy, while Night-Rider exploits the geometric center, leading to inaccurate constraints.
- 6) A robust tracking recovery module design. Night-Rider relies on a single image to determine the correct match for pose recovery, whereas Night-Voyager leverages the information accumulated over a short period.

In summary, the contributions of this work are as follows:

- 1) An innovative object map-empowered nocturnal vision-aided state estimation framework is developed to achieve object-level correspondences, which essentially resolve bottlenecks and the crux in nocturnal visual tasks. Notably, this work bridges the critical gap in nocturnal visual state estimation.
- 2) A robust two-stage cross-modal data association approach is introduced, which effectively addresses the challenge of cross-modal correspondences between visual measurements and prior maps.
- 3) A hierarchical initialization method, efficiently solving the global localization problem within the map, is proposed without the aid of manual intervention or GNSS.
- 4) A novel matrix Lie group formulation and a feature-decoupled MSC-InEKF are designed, equipping Night-Voyager with a consistent and efficient state estimator. In addition, multiple state representations are thoroughly compared via an in-depth observability analysis.
- 5) To foster research and field applications, the code and the nocturnal multi-sensor dataset are publicly released.

Ultimately, the proposed Night-Voyager framework endows robots with extraordinary localization capabilities, enabling reliable autonomous navigation in nighttime urban environments and substantially expanding the applicability of such systems for round-the-clock operations.



## II. RELATED WORK

In this section, we discuss the most related research works on priori LiDAR map-based visual localization, along with nocturnal visual state estimation and SLAM.

### A. LiDAR Map-based Visual Localization

Due to the long-term stability and rich geometric information of LiDAR maps, cross-modal localization attracts substantial research attention. Early research works focus on comparing the similarity between images and projected LiDAR data by utilizing normalized mutual information (NMI) [47], normalized information distance (NID) [48], intensity [49], and depth [50], [51]. Some methods [52]–[55] propose to transform the 2D-3D matching problem into a 3D-3D matching problem, thus the structure information can be utilized. Caselitz et al. [53] employ a visual odometry algorithm to reconstruct 3D points from visual features. The sparse reconstructed points are matched with the map for tracking. In [54], semantic consistency between visual features and maps is introduced to improve the accuracy of point-to-plane Iterative Closest Point (ICP) problems. Structural features (e.g., lines) [56]–[58] are also utilized for sufficient matches. Recently, deep learning techniques are introduced into cross-modal localization tasks [59]–[65]. While these methods achieve reasonable accuracy, they necessitate dense maps and abundant visual information for cross-modal correspondences, which can be challenging to apply in nighttime scenes.

To alleviate the huge memory cost of dense maps, common landmarks (e.g., lanes, poles, signboards) are utilized to establish lightweight maps [66]–[69]. In [67], the authors leverage semantic segmentation and a distance transformation method for data association. Liao et al. [68] develop a coarse-to-fine localization method, using the coarse pose from wheel odometry to perform the data association of poles and refining the pose from matches. Wang et al. [69] propose a new data association method that exploits the local structure, global pattern, and temporal consistency. Compared to the landmarks utilized in the aforementioned works, streetlights are stable, salient, and easily detectable in low-illumination environments, making them suitable for nighttime visual localization.

### B. Nocturnal Visual State Estimation and SLAM

Conventional visual-inertial odometry (VIO) and vision-aided SLAM methods [2]–[9], [70], [71], such as VINS-Mono [3] and Multi-State-Constraint Extended Kalman Filter (MSCKF) [2], [72], typically rely on pixel-level features from images. Unfortunately, these methods struggle in nocturnal environments [11], as discussed in Section I-B. Thanks to the power of data-driven machine learning techniques, methods for low-light image enhancement [22]–[27], [73], [74] are developed to improve feature extraction. In [73], a deep neural network is designed to generate more informative images for visual odometry (VO). Jung et al. [74] further improve the VO by introducing temporal and spatial constraints into the neural network. However, the issues of generalization and heavy computational burden significantly hinder the application of

these methods in robotic tasks. Moreover, some studies focus on designing robust descriptors [75], [76], explicitly modeling camera parameters using photometric models [6], [8], [18], [77], and controlling camera attributes like exposure time and gain [10], [11], [17], [78]–[80]. In [11], an exposure control scheme that considers inter-frame consistency is proposed, which effectively increases the matched features for visual SLAM. This work is further extended by jointly considering exposure time and gain [10]. Nevertheless, these approaches require an in-depth understanding of the specific sensor and heuristic tuning of parameters, which impedes their generalization to different setups. In addition, these methods still essentially rely on pixel-level correspondences, which cannot resolve the fundamental *insufficiency* and *inconsistency* issues in nocturnal visual state estimation, as discussed in Section I-B. Few studies investigate consistent and stable visual features for nocturnal state estimation. Nelson et al. [81] propose NightNav, a visual localization system that uses a prior map storing streetlight images from different views and positions. However, the assumption that the area of streetlight blobs is inversely proportional to the distance of streetlights from the camera is overly stringent. When occlusion and perspective change cases occur, the distance-area function is unreliable. Besides, the pre-stored images of all streetlights in NightNav increase the storage requirement. Our previous work, Night-Rider [46], only uses the object-level visual association from streetlights, demonstrating accurate localization performance within the streetlight map. However, Night-Rider ignores historical information and suffers from degradation and degeneration cases. Additionally, Night-Rider can only be applied in nighttime scenes rather than all-day scenarios.

In this work, a novel state estimation framework named Night-Voyager is proposed, leveraging hybrid object-level and pixel-level visual correspondences to tackle the fundamental bottlenecks of *insufficiency* and *inconsistency* in nocturnal visual cases, thereby addressing the critical crux inherent in mainstream pixel-level methodologies.

## III. PRELIMINARY AND STATE DEFINITION

### A. Theoretical Background

**Lie Group and Lie Algebra:** Let  $\mathcal{G}$  denote a matrix Lie group with its corresponding Lie algebra  $\mathfrak{g}$ . Elements in the Euclidean space can be mapped to the Lie group by the exponential mapping  $\text{Exp} : \mathbb{R}^{dim_{\mathfrak{g}}} \rightarrow \mathcal{G}$  [82]:

$$\mathbf{X} = \text{Exp}(\xi) = \exp(\xi^{\wedge}) \quad (1)$$

where  $dim_{\mathfrak{g}}$  represents the dimension of the Euclidean space of Lie algebra.  $\xi \in \mathbb{R}^{dim_{\mathfrak{g}}}$  and  $\mathbf{X} \in \mathcal{G}$  are the elements in the corresponding Euclidean space and Lie group.  $\exp(\cdot)$  is the standard exponential map.  $(\cdot)^{\wedge} : \mathbb{R}^{dim_{\mathfrak{g}}} \rightarrow \mathfrak{g}$  converts the vector representation to the isomorphic matrix representation of the Lie algebra. We denote  $\text{Log} : \mathcal{G} \rightarrow \mathbb{R}^{dim_{\mathfrak{g}}}$  as the inverse operation that maps the Lie group to the Euclidean space.

The commonly used Lie groups include the special orthogonal groups  $SO(3)$ , the special Euclidean groups  $SE(3)$ , and the extended special Euclidean group  $SE_2(3)$ , which is an



extension of  $SE(3)$ , containing a rotation matrix and two vectors. It is possible to extend the Lie groups  $SE(3)$  or  $SE_2(3)$  by associating them with  $K$  additional vectors, resulting in the Lie groups  $SE_{1+K}(3)$  or  $SE_{2+K}(3)$ , respectively [83].

**Invariant Error:** Suppose  $\mathbf{X} \in \mathcal{G}$  and  $\hat{\mathbf{X}} \in \mathcal{G}$  are, respectively, the true and estimated states, the left- and right-invariant errors are defined as [82]:

$$\boldsymbol{\eta}^l = \mathbf{X}^{-1}\hat{\mathbf{X}} \quad (\text{Left-invariant Error}) \quad (2)$$

$$\boldsymbol{\eta}^r = \hat{\mathbf{X}}\mathbf{X}^{-1} \quad (\text{Right-invariant Error}). \quad (3)$$

In this work, we use the right-invariant error representation [83]–[85] to formulate the state estimation problem.

### B. Notation and State Definition

In this work,  $^G(\cdot)$ ,  $^L(\cdot)$ ,  $^C(\cdot)$ ,  $^O(\cdot)$ , and  $^I(\cdot)$  respectively represent a 3D vector in the global map, local, camera, odometer, and Inertial Measurement Unit (IMU) frames. Both the map and local frames are fixed, and the  $z$  direction of the local frame is aligned with the constant gravity vector  $\mathbf{g}$ . To distinguish the frames between mapping and online state estimation, we use primed letters to represent the frames in the mapping system, e.g.,  $I'$ . The IMU frame coincides with the body frame.  $^L\mathbf{T}_I \in SE(3)$  is the transformation from the local frame to body frame, including the rotation  $^L\mathbf{R}_I \in SO(3)$  and the position  $^L\mathbf{p}_I \in \mathbb{R}^3$ . All velocities are with respect to the local frame.  $^L\mathbf{v}_I \in \mathbb{R}^3$  is the velocity of the body frame with respect to the local frame. Time index  $k$  and IMU sample index  $i$  indicate their corresponding time  $t_k$  and  $t_i$ .  $(\cdot)$  and  $(\cdot)$  represent the measurement and the state estimate, respectively.

The map-based state estimation problem is decomposed into two key parts: estimating odometry in the local frame and determining the relative transformation from the local frame to the map frame. Thus, the system state  $\mathbf{X}_k$  at time  $t_k$  is divided into: the local state  $\mathbf{X}_{L_k}$  (including the body navigation state  $\mathbf{X}_{I_k} \in SE_2(3)$ , the IMU bias  $\mathbf{B}_k \in \mathbb{R}^6$ , and the historical pose clone  $\mathbf{X}_{C_k}$ ) and the compound state  $\mathbf{X}_{G_k} \in SE_{1+K}(3)$ :

$$\begin{aligned} \mathbf{X}_k &= (\mathbf{X}_{L_k}, \mathbf{X}_{G_k}) \\ \mathbf{X}_{L_k} &= (\mathbf{X}_{I_k}, \mathbf{B}_k, \mathbf{X}_{C_k}) \\ \mathbf{X}_{I_k} &= \begin{bmatrix} ^L\mathbf{R}_{I_k} & ^L\mathbf{p}_{I_k} & ^L\mathbf{v}_{I_k} \\ \mathbf{0}_{2 \times 3} & \mathbf{I}_{2 \times 2} & \end{bmatrix}, \mathbf{B}_k = [\mathbf{b}_{g_k}^\top \quad \mathbf{b}_{a_k}^\top]^\top \\ \mathbf{X}_{C_k} &= (\mathbf{X}_{CP_{j_k}}, \dots, \mathbf{X}_{CP_{j_k-c+1}}), \mathbf{X}_{CP_{j_k}} = \begin{bmatrix} ^L\mathbf{R}_{I_{j_k}} & ^L\mathbf{p}_{I_{j_k}} \\ \mathbf{0}_{1 \times 3} & 1 \end{bmatrix} \\ \mathbf{X}_{G_k} &= \begin{bmatrix} ^L\mathbf{R}_{G_k} & ^L\mathbf{p}_{G_k} & ^L\mathbf{p}_{f_{1_k}} & \dots & ^L\mathbf{p}_{f_{K_k}} \\ \mathbf{0}_{(1+K) \times 3} & \mathbf{I}_{(1+K) \times (1+K)} & \end{bmatrix} \quad (4) \end{aligned}$$

where  $^L\mathbf{R}_{I_k} \in SO(3)$ ,  $^L\mathbf{p}_{I_k} \in \mathbb{R}^3$ , and  $^L\mathbf{v}_{I_k} \in \mathbb{R}^3$  represent the rotation, position, and velocity of body frame in the local frame, respectively. The bias state includes the gyroscope bias  $\mathbf{b}_{g_k} \in \mathbb{R}^3$  and the accelerometer bias  $\mathbf{b}_{a_k} \in \mathbb{R}^3$ . The state also contains  $c$  historical IMU pose clones  $\mathbf{X}_{CP_{j_k}} \in SE(3)$ ,  $j = k - c + 1, \dots, k$ , each consists of a rotation matrix  $^L\mathbf{R}_{I_{j_k}} \in SO(3)$  and a translation vector  $^L\mathbf{p}_{I_{j_k}} \in \mathbb{R}^3$ . The index  $j_k$  denotes the pose cloned at time  $t_{j_k}$  with the estimate at  $t_k$ .  $\mathbf{X}_{G_k}$  is composed of the rotation  $^L\mathbf{R}_{G_k} \in SO(3)$  and position  $^L\mathbf{p}_{G_k} \in \mathbb{R}^3$  of global map frame with respect to the local

frame, as well as the positions of the tracked feature points expressed in the local frame  $^L\mathbf{p}_{f_{l_k}} \in \mathbb{R}^3$ ,  $l = 1, \dots, K$ .

The right-invariant error in (3) between the estimated state  $\hat{\mathbf{X}}_k$  and the true state  $\mathbf{X}_k$  is leveraged to derive [84]:

$$\begin{aligned} ^L\mathbf{R}_{I_k} &= \text{Exp}(\boldsymbol{\xi}_{R_{LI_k}}) ^L\hat{\mathbf{R}}_{I_k} \\ ^L\mathbf{p}_{I_k} &= \text{Exp}(\boldsymbol{\xi}_{R_{LI_k}}) ^L\hat{\mathbf{p}}_{I_k} + \mathbf{J}_l(\boldsymbol{\xi}_{R_{LI_k}}) \boldsymbol{\xi}_{p_{LI_k}} \\ ^L\mathbf{v}_{I_k} &= \text{Exp}(\boldsymbol{\xi}_{R_{LI_k}}) ^L\hat{\mathbf{v}}_{I_k} + \mathbf{J}_l(\boldsymbol{\xi}_{R_{LI_k}}) \boldsymbol{\xi}_{v_{LI_k}} \\ ^L\mathbf{R}_{I_{j_k}} &= \text{Exp}(\boldsymbol{\xi}_{R_{CP_{j_k}}}) ^L\hat{\mathbf{R}}_{I_{j_k}} \\ ^L\mathbf{p}_{I_{j_k}} &= \text{Exp}(\boldsymbol{\xi}_{R_{CP_{j_k}}}) ^L\hat{\mathbf{p}}_{I_{j_k}} + \mathbf{J}_l(\boldsymbol{\xi}_{R_{CP_{j_k}}}) \boldsymbol{\xi}_{p_{CP_{j_k}}} \\ ^L\mathbf{R}_{G_k} &= \text{Exp}(\boldsymbol{\xi}_{R_{LG_k}}) ^L\hat{\mathbf{R}}_{G_k} \\ ^L\mathbf{p}_{G_k} &= \text{Exp}(\boldsymbol{\xi}_{R_{LG_k}}) ^L\hat{\mathbf{p}}_{G_k} + \mathbf{J}_l(\boldsymbol{\xi}_{R_{LG_k}}) \boldsymbol{\xi}_{p_{LG_k}} \\ ^L\mathbf{p}_{f_{l_k}} &= \text{Exp}(\boldsymbol{\xi}_{R_{LG_k}}) ^L\hat{\mathbf{p}}_{f_{l_k}} + \mathbf{J}_l(\boldsymbol{\xi}_{R_{LG_k}}) \boldsymbol{\xi}_{p_{Lf_{l_k}}} \\ \mathbf{b}_{g_k} &= \hat{\mathbf{b}}_{g_k} + \delta \mathbf{b}_{g_k}, \quad \mathbf{b}_{a_k} = \hat{\mathbf{b}}_{a_k} + \delta \mathbf{b}_{a_k} \quad (5) \end{aligned}$$

where  $\boldsymbol{\xi}_{I_k} = [\boldsymbol{\xi}_{R_{LI_k}}^\top \quad \boldsymbol{\xi}_{p_{LI_k}}^\top \quad \boldsymbol{\xi}_{v_{LI_k}}^\top]^\top \in \mathbb{R}^9$  is the body error state. The subscript  $(\cdot)_{R_{LI_k}}$  indicates that the error state  $\boldsymbol{\xi}_{R_{LI_k}}$  corresponds to the rotation state  $^L\mathbf{R}_{I_k}$ ,  $(\cdot)_{p_{LI_k}}$  indicates that the error state  $\boldsymbol{\xi}_{p_{LI_k}}$  corresponds to the position state  $^L\mathbf{p}_{I_k}$ , and  $(\cdot)_{v_{LI_k}}$  indicates that the error state  $\boldsymbol{\xi}_{v_{LI_k}}$  corresponds to the velocity state  $^L\mathbf{v}_{I_k}$ .  $\boldsymbol{\xi}_{C_k} = [\boldsymbol{\xi}_{CP_{j_k}}^\top \dots \boldsymbol{\xi}_{CP_{j_k-c+1}}^\top]^\top \in \mathbb{R}^{6c}$  contains all the error states of pose clones, with each one formulated as  $\boldsymbol{\xi}_{CP_{j_k}} = [\boldsymbol{\xi}_{R_{CP_{j_k}}}^\top \quad \boldsymbol{\xi}_{p_{CP_{j_k}}}^\top]^\top \in \mathbb{R}^6$ .  $\boldsymbol{\xi}_{G_k} = [\boldsymbol{\xi}_{R_{LG_k}}^\top \quad \boldsymbol{\xi}_{p_{LG_k}}^\top \quad \boldsymbol{\xi}_{p_{Lf_{1_k}}}^\top \dots \boldsymbol{\xi}_{p_{Lf_{K_k}}}^\top]^\top \in \mathbb{R}^{6+3K}$  is the compound error state, where  $\boldsymbol{\xi}_{R_{LG_k}} = [\boldsymbol{\xi}_{R_{LG_k}}^\top \quad \boldsymbol{\xi}_{p_{LG_k}}^\top]^\top \in \mathbb{R}^6$  denotes the error state of relative transformation and  $\boldsymbol{\xi}_{p_{Lf_{l_k}}} \in \mathbb{R}^3$  is the feature error state.  $\boldsymbol{\zeta}_{B_k} = [\delta \mathbf{b}_{g_k}^\top \quad \delta \mathbf{b}_{a_k}^\top]^\top \in \mathbb{R}^6$  represents the bias error state.  $\mathbf{J}_l(\cdot)$  denotes the left Jacobian of  $SO(3)$  [86]. The error state  $\boldsymbol{\xi}_k = [\boldsymbol{\xi}_{I_k}^\top \quad \boldsymbol{\zeta}_{B_k}^\top \quad \boldsymbol{\xi}_{C_k}^\top \quad \boldsymbol{\xi}_{G_k}^\top]^\top \in \mathbb{R}^{21+6c+3K}$  is used to formulate the state estimation problem in the following sections. For simplicity, we only use one feature point  $^L\mathbf{p}_{f_k}$  to formulate the state in the rest sections.

## IV. MULTI-SENSOR FUSION MODULE

We introduce the multi-sensor fusion module (MSF), a general module for vision-aided state estimation, fusing multi-sensor measurements in a tightly-coupled scheme.

### A. State Propagation

The system dynamics for state propagation can be derived from the IMU kinematic model [87] as:

$$\begin{cases} ^L\dot{\mathbf{R}}_I = ^L\mathbf{R}_I(\tilde{\boldsymbol{\omega}} - \mathbf{b}_g - \mathbf{n}_g)_\times, & ^L\dot{\mathbf{p}}_I = ^L\mathbf{v}_I \\ ^L\dot{\mathbf{v}}_I = ^L\mathbf{R}_I(\tilde{\mathbf{a}} - \mathbf{b}_a - \mathbf{n}_a) + \mathbf{g}, & \dot{\mathbf{b}}_g = \mathbf{n}_{bg}, \quad \dot{\mathbf{b}}_a = \mathbf{n}_{ba} \\ ^L\dot{\mathbf{R}}_{I_j} = \mathbf{0}_{3 \times 3}, & ^L\dot{\mathbf{p}}_{I_j} = \mathbf{0}_{3 \times 1}, \quad j = k, \dots, k - c + 1 \\ ^L\dot{\mathbf{R}}_G = \mathbf{0}_{3 \times 3}, & ^L\dot{\mathbf{p}}_G = \mathbf{0}_{3 \times 1}, \quad ^L\dot{\mathbf{p}}_f = \mathbf{0}_{3 \times 1} \end{cases} \quad (6)$$

where  $\tilde{\boldsymbol{\omega}}$  and  $\tilde{\mathbf{a}}$  represent IMU readings of angular velocity and specific force, contaminated respectively by Gaussian noises  $\mathbf{n}_g$  and  $\mathbf{n}_a$ .  $(\cdot)_\times$  is the 3-dimensional skew-symmetric matrix.  $\mathbf{n}_{bg}$  and  $\mathbf{n}_{ba}$  are the random walk noises of IMU biases. The

discrete system dynamics can be derived by integrating IMU measurements from  $t_i$  to  $t_{i+1}$ :

$$\begin{cases} {}^L\mathbf{R}_{I_{i+1}} = {}^L\mathbf{R}_{I_i}\Delta\mathbf{R}_i \\ {}^L\mathbf{p}_{I_{i+1}} = {}^L\mathbf{p}_{I_i} + {}^L\mathbf{v}_{I_i}\delta t + {}^L\mathbf{R}_{I_i}\Delta\mathbf{p}_i + \frac{1}{2}\mathbf{g}\delta t^2 \\ {}^L\mathbf{v}_{I_{i+1}} = {}^L\mathbf{v}_{I_i} + {}^L\mathbf{R}_{I_i}\Delta\mathbf{v}_i + \mathbf{g}\delta t \\ \mathbf{b}_{g_{i+1}} = \mathbf{b}_{g_i} + \int_{t_i}^{t_{i+1}} \mathbf{n}_{bg}d\tau, \quad \mathbf{b}_{a_{i+1}} = \mathbf{b}_{a_i} + \int_{t_i}^{t_{i+1}} \mathbf{n}_{ba}d\tau \end{cases} \quad (7)$$

where  $\Delta\mathbf{R}_i = \text{Exp}(\int_{t_i}^{t_{i+1}} \boldsymbol{\omega}_\tau d\tau)$ ,  $\Delta\mathbf{v}_i = \int_{t_i}^{t_{i+1}} {}^{I_i}\mathbf{R}_{I_\tau} \mathbf{a}_\tau d\tau$ , and  $\Delta\mathbf{p}_i = \int_{t_i}^{t_{i+1}} \int_{t_i}^s {}^{I_i}\mathbf{R}_{I_\tau} \mathbf{a}_\tau d\tau ds$ .  $\delta t = t_{i+1} - t_i$  is the time interval. Following [86], we use the analytical combined IMU integration method to approximate  $\Delta\mathbf{R}_i$ ,  $\Delta\mathbf{p}_i$ ,  $\Delta\mathbf{v}_i$ , and substitute the error-state functions (5) into (7) to derive the linearized error propagation function as:

$$\begin{aligned} \boldsymbol{\xi}_{i+1} &= \begin{bmatrix} \boldsymbol{\xi}_{I_{i+1}} \\ \boldsymbol{\xi}_{B_{i+1}} \\ \boldsymbol{\xi}_{C_{i+1}} \\ \boldsymbol{\xi}_{T_{LG_{i+1}}} \\ \boldsymbol{\xi}_{p_{Lf_{i+1}}} \end{bmatrix} = \boldsymbol{\Phi}_i^{i+1} \begin{bmatrix} \boldsymbol{\xi}_{I_i} \\ \boldsymbol{\xi}_{B_i} \\ \boldsymbol{\xi}_{C_i} \\ \boldsymbol{\xi}_{T_{LG_i}} \\ \boldsymbol{\xi}_{p_{Lf_i}} \end{bmatrix} + \mathbf{G}_i \begin{bmatrix} \mathbf{n}_{dg} \\ \mathbf{n}_{da} \\ \mathbf{n}_{dbg} \\ \mathbf{n}_{dba} \end{bmatrix} \quad (8) \\ \boldsymbol{\Phi}_i^{i+1} &= \begin{bmatrix} \boldsymbol{\Phi}_{II} & \boldsymbol{\Phi}_{IB} & \mathbf{0}_{9 \times 6c} & \mathbf{0}_{9 \times 6} & \mathbf{0}_{9 \times 3} \\ \mathbf{0}_{6 \times 9} & \mathbf{I}_{6 \times 6} & \mathbf{0}_{6 \times 6c} & \mathbf{0}_{6 \times 9} & \mathbf{0}_{6 \times 3} \\ \mathbf{0}_{6c \times 9} & \mathbf{0}_{6c \times 6} & \mathbf{I}_{6c \times 6c} & \mathbf{0}_{6c \times 9} & \mathbf{0}_{6c \times 3} \\ \mathbf{0}_{6 \times 9} & \mathbf{0}_{6 \times 6} & \mathbf{0}_{6 \times 6c} & \mathbf{I}_{6 \times 6} & \mathbf{0}_{6 \times 3} \\ \mathbf{0}_{3 \times 9} & \mathbf{0}_{3 \times 6} & \mathbf{0}_{3 \times 6c} & \mathbf{0}_{3 \times 6} & \mathbf{I}_{3 \times 3} \end{bmatrix} \mathbf{G}_i = \begin{bmatrix} \mathbf{G}_{II} & \mathbf{0}_{9 \times 6} \\ \mathbf{0}_{6 \times 6} & \mathbf{I}_{6 \times 6} \delta t \\ \mathbf{0}_{6c \times 6} & \mathbf{0}_{6c \times 6} \\ \mathbf{0}_{6 \times 6} & \mathbf{0}_{6 \times 6} \\ \mathbf{0}_{3 \times 6} & \mathbf{0}_{3 \times 6} \end{bmatrix} \end{aligned}$$

where  $\boldsymbol{\Phi}_i^{i+1} \in \mathbb{R}^{(21+6c+3) \times (21+6c+3)}$  and  $\mathbf{G}_i \in \mathbb{R}^{(21+6c+3) \times 12}$  are respectively the transition matrix and the noise Jacobian matrix.  $\mathbf{n}_d = [\mathbf{n}_{dg}^\top \quad \mathbf{n}_{da}^\top \quad \mathbf{n}_{dbg}^\top \quad \mathbf{n}_{dba}^\top]^\top$  is the discretized noise. The matrix block components are formulated as:

$$\begin{aligned} \boldsymbol{\Phi}_{II} &= \begin{bmatrix} \mathbf{I}_{3 \times 3} & \mathbf{0}_{3 \times 3} & \mathbf{0}_{3 \times 3} \\ \frac{1}{2}(\mathbf{g}) \times \delta t^2 & \mathbf{I}_{3 \times 3} & \mathbf{I}_{3 \times 3} \delta t \\ (\mathbf{g}) \times \delta t & \mathbf{0}_{3 \times 3} & \mathbf{I}_{3 \times 3} \end{bmatrix} \quad (9) \\ \boldsymbol{\Phi}_{IB} = \mathbf{G}_{II} &= \begin{bmatrix} -\Delta\mathbf{R}\mathbf{J} & \mathbf{0}_{3 \times 3} \\ -(^L\hat{\mathbf{p}}_{I_{i+1}}) \times \Delta\mathbf{R}\mathbf{J} + ^L\hat{\mathbf{R}}_{I_i}\boldsymbol{\Xi}_4 - ^L\hat{\mathbf{R}}_{I_i}\boldsymbol{\Xi}_2 \\ -(^L\hat{\mathbf{v}}_{I_{i+1}}) \times \Delta\mathbf{R}\mathbf{J} + ^L\hat{\mathbf{R}}_{I_i}\boldsymbol{\Xi}_3 - ^L\hat{\mathbf{R}}_{I_i}\boldsymbol{\Xi}_1 \end{bmatrix} \end{aligned}$$

where  $\Delta\mathbf{R}\mathbf{J} = ^L\hat{\mathbf{R}}_{I_{i+1}} \mathbf{J}_r(\text{Log}(\Delta\hat{\mathbf{R}}_i))\delta t$  with  $\mathbf{J}_r(\cdot)$  denoting the right Jacobian of  $SO(3)$  [86].  $\boldsymbol{\Xi}_1, \boldsymbol{\Xi}_2, \boldsymbol{\Xi}_3, \boldsymbol{\Xi}_4$  are the integration components and their formulations can be found in [88]. More derivation details are provided in the corresponding supplementary material (in the GitHub repository).

Consequently, the estimated state  $\hat{\mathbf{X}}_i$  and covariance  $\hat{\mathbf{P}}_i$  are propagated to time  $t_{i+1}$  by:

$$\begin{cases} ^L\hat{\mathbf{R}}_{I_{i+1}} = ^L\hat{\mathbf{R}}_{I_i} \text{Exp}((\tilde{\boldsymbol{\omega}}_i - \hat{\mathbf{b}}_{\omega_i})\delta t) \\ ^L\hat{\mathbf{p}}_{I_{i+1}} = ^L\hat{\mathbf{p}}_{I_i} + ^L\hat{\mathbf{v}}_{I_i}\delta t + ^L\hat{\mathbf{R}}_{I_{i+1}}\boldsymbol{\Xi}_2(\tilde{\mathbf{a}}_i - \hat{\mathbf{b}}_{a_i}) + \frac{1}{2}\mathbf{g}\delta t^2 \\ ^L\hat{\mathbf{v}}_{I_{i+1}} = ^L\hat{\mathbf{v}}_{I_i} + ^L\hat{\mathbf{R}}_{I_i}\boldsymbol{\Xi}_1(\tilde{\mathbf{a}}_i - \hat{\mathbf{b}}_{a_i}) + \mathbf{g}\delta t \\ \hat{\mathbf{b}}_{g_{i+1}} = \hat{\mathbf{b}}_{g_i}, \quad \hat{\mathbf{b}}_{a_{i+1}} = \hat{\mathbf{b}}_{a_i} \\ ^L\hat{\mathbf{R}}_{I_{j+1}} = ^L\hat{\mathbf{R}}_{I_{j_i}}, \quad ^L\hat{\mathbf{p}}_{I_{j+1}} = ^L\hat{\mathbf{p}}_{I_{j_i}}, \quad j = k, \dots, k-c+1 \\ ^L\hat{\mathbf{R}}_{G_{i+1}} = ^L\hat{\mathbf{R}}_{G_i}, \quad ^L\hat{\mathbf{p}}_{G_{i+1}} = ^L\hat{\mathbf{p}}_{G_i}, \quad ^L\hat{\mathbf{p}}_{f_{i+1}} = ^L\hat{\mathbf{p}}_{f_i} \\ \hat{\mathbf{P}}_{i+1} = \boldsymbol{\Phi}_i^{i+1} \hat{\mathbf{P}}_i \boldsymbol{\Phi}_i^{i+1\top} + \mathbf{G}_i \mathbf{Q}_d \mathbf{G}_i^\top \end{cases} \quad (10)$$

where  $\mathbf{Q}_d$  denotes the covariance of  $\mathbf{n}_d$ . The initial values of  $\hat{\mathbf{X}}_0$  and  $\hat{\mathbf{P}}_0$  at time  $t_i = t_0$  are set to the most recently updated state and covariance (obtained at the closest odometer or camera measurement time  $t_k$ ). The system state will be

propagated to  $t_{k+1}$  when a new odometer or camera measurement arrives. If the measurement is captured from camera, we augment  $\hat{\mathbf{X}}_{C_{k+1}}$  by cloning the body pose and the oldest clone will be marginalized after the state update.

### B. Odometer Observation

It is common to equip wheeled robots with odometers, which measure wheel rates and provide linear velocity measurements under the non-slip assumption. We assume the velocity measurement  ${}^O\tilde{\mathbf{v}}_{O_k}$  to be corrupted by the Gaussian white noise  $\mathbf{n}_{o_k} \sim \mathcal{N}(\mathbf{0}_{3 \times 1}, \boldsymbol{\Sigma}_o)$ :

$${}^O\tilde{\mathbf{v}}_{O_k} = {}^O\mathbf{v}_{O_k} + \mathbf{n}_{o_k}. \quad (11)$$

${}^O\mathbf{v}_{O_k}$  can be transformed from the velocity expressed in the body (IMU) frame  ${}^I\mathbf{v}_{I_k}$  through the calibrated extrinsic parameters  $({}^O\mathbf{R}_I, {}^O\mathbf{p}_I)$  between the odometer and body frame:

$${}^O\mathbf{v}_{O_k} = {}^O\mathbf{R}_I {}^I\mathbf{v}_{I_k} + ({}^O\mathbf{p}_I) \times {}^O\mathbf{R}_I (\tilde{\boldsymbol{\omega}}_k - \mathbf{b}_{g_k}). \quad (12)$$

In our system, the IMU and odometer are assumed to reside in the same location with only  ${}^O\mathbf{R}_I$  being considered, hence the odometer-based observation model is formulated as:

$$\tilde{\mathbf{y}}_{o_k} = {}^O\mathbf{R}_I {}^L\mathbf{R}_{I_k}^\top {}^L\mathbf{v}_{I_k} + \mathbf{n}_{o_k} \quad (13)$$

where  $\tilde{\mathbf{y}}_{o_k} = {}^O\tilde{\mathbf{v}}_{O_k}$  is the measured velocity in the odometer frame. With the error state functions in (5), we can linearize the measurement error with respect to  $\boldsymbol{\xi}_k$  as:

$$\mathbf{z}_{o_k} = \tilde{\mathbf{y}}_{o_k} - \hat{\mathbf{y}}_{o_k} \approx \mathbf{H}_{o_k} \boldsymbol{\xi}_k + \mathbf{n}_{o_k} \quad (14)$$

where  $\hat{\mathbf{y}}_{o_k}$  is the estimated velocity. The Jacobian  $\mathbf{H}_{o_k} \triangleq \frac{\partial \mathbf{z}_{o_k}}{\partial \boldsymbol{\xi}_k} \in \mathbb{R}^{3 \times (21+6c+3K)}$  can be found in the supplementary material. Using Kalman filtering theory [82], the updated states and covariance can be obtained.

### C. Feature Observation

The pixel-level visual features can provide effective supplementary constraints for nocturnal state estimation, especially when the streetlights are invisible. Additionally, leveraging visual features enables all-day localization. Features that are tracked longer than the size of sliding window are initialized into the active state through triangulation. For each observation of  ${}^L\mathbf{p}_{f_k}$  in pose clones, we have the following observation:

$$\tilde{\mathbf{y}}_{f_{j_k}} = \mathbf{h} \left( {}^C\mathbf{R}_I {}^L\mathbf{R}_{I_{j_k}}^\top ({}^L\mathbf{p}_{f_k} - {}^L\mathbf{p}_{I_{j_k}}) + {}^C\mathbf{p}_I \right) + \mathbf{n}_{f_k} \quad (15)$$

where  $\tilde{\mathbf{y}}_{f_{j_k}}$  denotes the 2D feature point measurement captured at time  $t_j$ .  $\mathbf{h}(\cdot)$  is the camera projection function.  $({}^C\mathbf{R}_I, {}^C\mathbf{p}_I)$  constitute the extrinsic parameters between camera and IMU.  $\mathbf{n}_{f_k} \sim \mathcal{N}(\mathbf{0}_{2 \times 1}, \boldsymbol{\Sigma}_{f_k})$  is the Gaussian noise. Then the linearized measurement error function is derived as:

$$\mathbf{z}_{f_{j_k}} = \tilde{\mathbf{y}}_{f_{j_k}} - \hat{\mathbf{y}}_{f_{j_k}} \approx \mathbf{H}_{f_{j_k}} \boldsymbol{\xi}_k + \mathbf{n}_{f_k} \quad (16)$$

where  $\mathbf{H}_{f_{j_k}} \triangleq \frac{\partial \mathbf{z}_{f_{j_k}}}{\partial \boldsymbol{\xi}_k} \in \mathbb{R}^{2 \times (21+6c+3K)}$  is the observation Jacobian matrix. By stacking all observations from different pose clones, the state and covariance can be updated. Detailed formulations of matrix blocks and corresponding derivations can be found in the supplementary material.

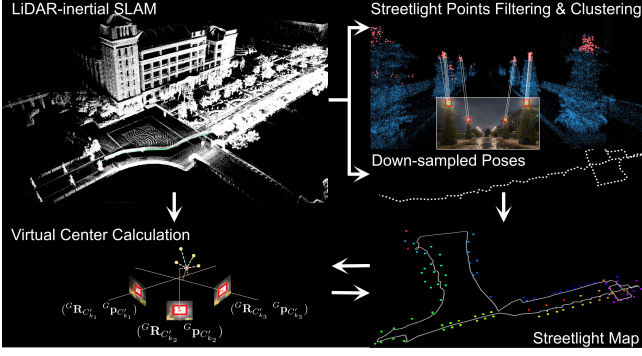


Fig. 4: Generation process of the streetlight map. The points of each LiDAR scan are projected onto the image and the streetlight points are filtered according to streetlight detections in the image. The final streetlight map is constructed by clustering the streetlight points and storing the poses estimated during the mapping process. With the streetlight map, the LiDAR-inertial SLAM is run again to calculate the virtual center of each streetlight cluster.

## V. MAP-BASED LOCALIZATION

The essential component for achieving accurate nocturnal visual state estimation is the object-level streetlight map. This section details the generation of the streetlight map and virtual centers, the process of streetlight association and observation, along with the prior pose observation. The map comprises 3D points of streetlights, prior poses generated during the mapping process, and virtual centers of streetlight clusters. The first two can provide prior information, while the virtual centers enable more accurate modeling for visual constraints.

### A. Streetlight Map and Virtual Center Generation

The streetlight mapping process is shown in Fig. 4. We employ an image-based object detection method [89] to filter luminous streetlight points from LiDAR measurements to construct the streetlight map. For each LiDAR scan, points whose projections fall into the detection boxes are labeled as “streetlight”. The original LiDAR map is generated using a modified LiDAR-inertial SLAM system [90], improved with a fast and accurate loop closure detection method [91] and a back-end optimization module [92]. The map points with “streetlight” labels [46] and the prior poses estimated during the mapping process are retained. The final neat 3D streetlight map is displayed in the right bottom of Fig. 4 where the colored blocks denote streetlights and the white dotted line indicates the prior poses. Since the mapping process is offline, one can also fuse additional sensors like GNSS to obtain a more accurate and consistent map. With the streetlight map, we can generate virtual centers for map-based localization.

It is naive to directly use geometric centers of streetlight clusters and detection box centers to constrain the state. However, as Fig. 5 shows, they do not satisfy the reprojection constraint, which inevitably influences the state estimation accuracy. The main reasons are twofold: 1) the centers of light bulbs are not exactly consistent with those of streetlight clusters, and 2) it is difficult to reconstruct the complete shape of streetlights, thus making the centers of streetlight clusters deviate from the true geometric centers. Therefore, we propose



Fig. 5: The projected geometric centers often deviate from streetlight observation centers. The red, blue, and brown crosses are the projected geometric centers, virtual centers, and detection box centers.

the virtual center, which is calculated from both the LiDAR and image data during the mapping process.

When performing LiDAR-inertial SLAM for the second time, the nearby streetlight clusters are projected onto the image according to the estimated pose. If all the projected points of a streetlight cluster lie within a bounding box, it is considered matching with the streetlight cluster. Therefore, the detection boxes from multiple viewpoints corresponding to a specific streetlight cluster are collected. Suppose there are  $Q$  points and  $V$  detection boxes from  $V$  different views belonging to a streetlight cluster, a distance function of a virtual point  ${}^G\mathbf{c}_s$  is formulated as:

$$\frac{1}{Q} \sum_{q=1}^Q \|{}^G\mathbf{c}_s - {}^G\tilde{\mathbf{p}}_s^q\|_2^2 + \frac{\lambda}{V} \sum_{v=1}^V \frac{\|{}^G\tilde{\mathbf{n}}_v - {}^G\mathbf{c}_s \times {}^G\tilde{\mathbf{d}}_v\|_2^2}{\|{}^G\tilde{\mathbf{d}}_v\|_2^2} \quad (17)$$

where  ${}^G\tilde{\mathbf{p}}_s^q$  is the streetlight point. The first term represents the average distance from the virtual center to all streetlight points, and the second denotes the average distance from the virtual center to the back-projected rays of the detection box centers [93].  $\lambda$  is a weight to balance the influence of these two terms. We utilize the Plücker coordinates  ${}^G\tilde{\mathcal{P}}_v = [{}^G\tilde{\mathbf{a}}_v^\top \ {}^G\tilde{\mathbf{n}}_v^\top]^\top \in \mathbb{R}^6$  [93] to represent the back-projection line in the map frame, which is transformed from the camera frame by:

$${}^G\tilde{\mathcal{P}}_v = \text{Ad} \left( \begin{bmatrix} {}^G\tilde{\mathbf{R}}_{C'_v} & {}^G\tilde{\mathbf{p}}_{C'_v} \\ \mathbf{0}_{1 \times 3} & 1 \end{bmatrix} \right) \begin{bmatrix} \mathbf{K}^{-1} \tilde{\mathbf{p}}_{s_v} \\ \mathbf{0}_{3 \times 1} \end{bmatrix} \quad (18)$$

where  $({}^G\tilde{\mathbf{R}}_{C'_v}, {}^G\tilde{\mathbf{p}}_{C'_v})$  is the camera pose from the mapping SLAM system, and  $\text{Ad}(\cdot)$  denotes the adjoint matrix [94].  $\tilde{\mathbf{p}}_{s_v}$  is the homogeneous coordinate of the detection box center.  $\mathbf{K}$  represents the camera intrinsics matrix. By forcing the derivative of (17) to zero, the virtual center is calculated.

### B. Data Association and Streetlight Observation

Unlike feature points, designing descriptors for cross-modal data association is challenging. Therefore, we propose employing spatial information for data association, which has proven to be sufficiently effective. To maximize the association of image streetlight observations with the streetlight map, we propose a two-stage data association method by leveraging learning-based and binary-based detections.

1) *Learning-based Data Association:* In this stage, 2D streetlight observations are detected using an object detection network, such as [89]. Suppose that there are  $n_k$  detected boxes and  $m_k$  3D streetlight clusters near the robot’s current position. The detected bounding boxes are represented as  $\{\mathcal{B}_{d_k} = (\tilde{\mathbf{p}}_{s_{d_k}}, \tilde{\mathbf{l}}_{s_{d_k}})\}_{d=1}^{n_k}$  where  $\tilde{\mathbf{p}}_{s_{d_k}} = [\tilde{u}_{s_{d_k}} \ \tilde{v}_{s_{d_k}}]^\top$  is the image coordinate of the box center and  $\tilde{\mathbf{l}}_{s_{d_k}} = [\tilde{l}_{u_{s_{d_k}}} \ \tilde{l}_{v_{s_{d_k}}}]^\top$



contains the width and length of box. The streetlight clusters in the map are represented as  $\{\tilde{\mathcal{L}}_g = (\tilde{\mathbf{c}}_{s_g}^G, \tilde{\mathbf{p}}_{s_g}^1, \dots, \tilde{\mathbf{p}}_{s_g}^Q)\}_{g=1}^{m_k}$  where  $\tilde{\mathbf{c}}_{s_g}^G$  is the virtual center and  $\tilde{\mathbf{p}}_{s_g}^q \in \mathbb{R}^3, q = 1, \dots, Q$  denotes the 3D coordinate of each streetlight point. To handle potential false detections such as car headlights and reflective objects,  $(-1)$  is added to the set to indicate the absence of a matching streetlight cluster for any given detection. We score all combinations of streetlight matches and the one with the highest score is determined as the correct combination. The score is calculated based on the following two errors:

**Reprojection Error.** Given a pose, an incorrect match generally results in a large error between the box center and the projected virtual center of the streetlight cluster. We model and score the residual  $\mathbf{r}_{p,dg}$  using a Gaussian distribution. Then for the detected box  $\tilde{\mathcal{B}}_{d_k}$  and the streetlight cluster  $\tilde{\mathcal{L}}_{g_k}$ , the reprojection error-based score  $s_{p,dg}$  is calculated as:

$$s_{p,dg} = \mathcal{N}_1(\|\mathbf{r}_{p,dg}\|_2 | 0, \sigma_{p,dg}^2) \quad (19)$$

$$\mathbf{r}_{p,dg} = \tilde{\mathbf{p}}_{s_{d_k}} - \mathbf{h}(\tilde{\mathbf{c}}_{s_g}^C) \quad (20)$$

where  $\mathcal{N}_1(\|\mathbf{r}_{p,dg}\|_2 | 0, \sigma_{p,dg}^2)$  represents the one-dimensional Gaussian probability density function with mean 0 and variance  $\sigma_{p,dg}^2$ .  $\tilde{\mathbf{c}}_{s_g}^C = {}^C\mathbf{R}_I^L \tilde{\mathbf{R}}_{I_k}^\top ({}^L\tilde{\mathbf{R}}_{G_k} \tilde{\mathbf{c}}_{s_g}^G + {}^L\tilde{\mathbf{p}}_{G_k} - {}^L\tilde{\mathbf{p}}_{I_k}) + {}^C\mathbf{p}_I$  is the projected virtual center in the camera frame.

**Angle Error.** We also introduce the score  $s_{a,dg}$  based on angle error between the back-projection ray of the center of the box  $\tilde{\mathcal{B}}_{d_k}$  and the line connecting the virtual center of the streetlight cluster  $\tilde{\mathcal{L}}_{g_k}$  and the camera optical center:

$$s_{a,dg} = \mathcal{N}_1(\|\mathbf{r}_{a,dg}\|_2 | 0, \sigma_{a,dg}^2) \quad (21)$$

$$\mathbf{r}_{a,dg} = \frac{{}^C\tilde{\mathbf{p}}_{s_{d_k}} \times {}^C\tilde{\mathbf{c}}_{s_g}}{\|{}^C\tilde{\mathbf{p}}_{s_{d_k}}\|_2 \|{}^C\tilde{\mathbf{c}}_{s_g}\|_2} \quad (22)$$

where  ${}^C\tilde{\mathbf{p}}_{s_{d_k}} = \mathbf{h}^{-1}(\tilde{\mathbf{p}}_{s_{d_k}})$  is the back-projection ray.  $\sigma_{p,dg}^2$  and  $\sigma_{a,dg}^2$  are derived in the supplementary material.

The total score of each potential match is calculated by:

$$s_{dg} = \omega s_{p,dg} + (1 - \omega) s_{a,dg} \quad (23)$$

where  $0 \leq \omega \leq 1$  is the preset weight. For the streetlight  $\tilde{\mathcal{B}}_{d_k}$  without any correspondence, the score is calculated as  $s_{d(m_k+1)} = 1 - \sum_{g=1}^{m_k} s_{dg}$ .

Based on (23), each potential match is evaluated and assigned a score. We use  $l_{dg}$  to indicate whether the  $d$ -th streetlight observation matches the  $g$ -th 3D streetlight cluster.  $\tilde{\mathcal{D}}_k = \{((\tilde{\mathcal{B}}_{d_k}, \tilde{\mathcal{L}}_{g_k}) | l_{dg} = 1)\}_{d=1}^{n_k}$  denotes the possible match combinations. The set of clusters is augmented to  $m_k + n_k$ , where the extra  $n_k$  elements represent unmatched streetlight observations, i.e.,  $\tilde{\mathcal{B}}_{d_k}$  is assigned to  $(-1)$ . In this way,  $\tilde{\mathcal{D}}_k$  is made injective, meaning that each observation corresponds uniquely to one element in the set of clusters. To obtain the optimal combination  $\tilde{\mathcal{D}}_k^*$ , the problem is formulated as the classical assignment problem:

$$\tilde{\mathcal{D}}_k^* = \arg \max_{\tilde{\mathcal{D}}_k} \sum_{d=1}^{n_k} \sum_{g=1}^{m_k+n_k} l_{dg} s_{dg}, \text{ s.t. } \sum_{d=1}^{n_k} l_{dg} \leq 1, \sum_{g=1}^{m_k+n_k} l_{dg} = 1.$$

Using Hungarian algorithm [95], the optimization problem can be efficiently solved ( $\sim 0.2$  ms per frame). It should be noted that when there are few visible streetlights, the cumulative



Fig. 6: Examples of match extension. The red boxes represent the detection by the learning-based method and the green boxes are detected by the binary-based method. The images show that the learning-based method cannot detect small streetlights while the binary-based method makes up for this shortcoming.

error of state increases the above two match errors, making it possible to find no matches, i.e.,  $\tilde{\mathcal{D}}_k^* = \{(\tilde{\mathcal{B}}_{d_k}, -1)\}_{d=1}^{n_k}$ . However, since we model the score as a Gaussian distribution whose variance is related to the covariance of state, the increased covariance caused by few streetlights makes the proposed method able to accept matches with larger errors. In other words, our method can adaptively lower or raise the requirement for finding matches, which, to some extent, avoids the problem of tracking failure caused by few observations.

For each match of  $\tilde{\mathcal{D}}_k^*$ , the reprojection constraint between the virtual center  $\tilde{\mathbf{c}}_{s_g}^G$  of streetlight cluster and the box center  $\tilde{\mathbf{p}}_s$  of streetlight observation is formulated as:

$$\tilde{\mathbf{y}}_{s_k} = \mathbf{h}({}^C\mathbf{R}_I^L \tilde{\mathbf{R}}_{I_k}^\top ({}^L\tilde{\mathbf{R}}_{G_k} \tilde{\mathbf{c}}_{s_g}^G + {}^L\tilde{\mathbf{p}}_{G_k} - {}^L\tilde{\mathbf{p}}_{I_k}) + {}^C\mathbf{p}_I) + \mathbf{n}_{s_k} \quad (24)$$

where  $\tilde{\mathbf{y}}_{s_k} = \tilde{\mathbf{p}}_s$  and  $\mathbf{n}_{s_k} \sim \mathcal{N}(\mathbf{0}_{2 \times 1}, \Sigma_{s_k})$  is the Gaussian measurement noise. The linearized error function is:

$$\mathbf{z}_{s_k} = \tilde{\mathbf{y}}_{s_k} - \hat{\mathbf{y}}_{s_k} \approx \mathbf{H}_{s_k} \boldsymbol{\xi}_k + \mathbf{n}_{s_k} \quad (25)$$

where the Jacobian  $\mathbf{H}_{s_k} \triangleq \frac{\partial \mathbf{z}_{s_k}}{\partial \boldsymbol{\xi}_k} \in \mathbb{R}^{2 \times (21+6c+3K)}$ . Derivation details are provided in the supplementary material.

2) *Binary-based Data Association:* In the first stage, small streetlights are frequently missed by the object detection network, leading to the underutilization of potential streetlight matches. To remedy this issue, we introduce the binary-based streetlight detection method in the second stage. Fig. 6 shows the examples of match extension. Pixels with intensity above a specific threshold are processed by the contour tracing algorithm [96] to generate bounding boxes that represent streetlight observations. With the updated pose, all streetlight clusters without 2D matches are projected onto the image. For a single streetlight cluster, since the updated pose is relatively accurate, all boxes containing the projected points are considered as the candidate matches. For each box, we then calculate the ratio of the number of projected points within the box to the total point number within the cluster. The box with the maximum ratio is determined as the match for the cluster. By traversing all streetlight clusters, new matches are identified, enabling an update of the robot state. In addition, historical streetlight matches are preserved for state update. This strategy mitigates the impact of streetlight mismatches within the current frame, thereby enhancing robustness and accuracy.

### C. Prior Pose Observation

Since streetlights are commonly installed along both sides of roads, the wheeled robot is required to travel these roads multiple times to collect streetlights during the mapping process.

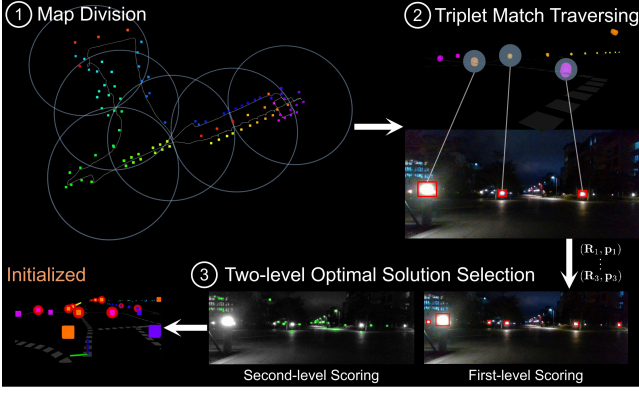


Fig. 7: Process of initialization. The streetlights are first divided into different regions according to the sampled prior poses. Next, all possible triplet matches are fed into the P3P algorithm [45] concurrently for solving the corresponding poses. The optimal solution is ultimately selected based on the designed two-level scoring strategy.

When the robot is in operation, it typically navigates along the nearby roads, resulting in similar trajectories in mapping and localization. This similarity inspires us to preserve the accurately estimated poses during mapping. These prior poses are leveraged in three ways: 1) Provide constraints for localization. 2) Divide the streetlight map into different regions to accelerate initialization. 3) Exclude unreasonable solutions in the initialization and tracking recovery modules. The last two points are elaborated on in Section VI and Section VII and this section focuses on the first point.

Using the estimated poses  ${}^L\hat{\mathbf{T}}_{I_k}$  and  ${}^L\hat{\mathbf{T}}_{G_k}$ , radius search is first conducted to identify the nearby prior poses. The prior poses  ${}^G\tilde{\mathbf{T}}_{I'} = ({}^G\tilde{\mathbf{R}}_{I'}, {}^G\tilde{\mathbf{p}}_{I'})$  within a threshold distance from the current pose, i.e.,  $\|{}^L\hat{\mathbf{R}}_{G_k}^\top ({}^L\hat{\mathbf{p}}_{I_k} - {}^L\hat{\mathbf{p}}_{G_k}) - {}^G\tilde{\mathbf{p}}_{I'}\| < \sigma$ , are selected to impose planar constraints. We assume that the road surface is locally planar, thus the constraint is:

$$\tilde{\mathbf{y}}_{p_k} = \begin{bmatrix} ({}^G\tilde{\mathbf{R}}_{I'}^\top {}^O\mathbf{R}_I^\top \mathbf{e}_3)^\top ({}^L\hat{\mathbf{R}}_{G_k}^\top ({}^L\hat{\mathbf{p}}_{I_k} - {}^L\hat{\mathbf{p}}_{G_k}) - {}^G\tilde{\mathbf{p}}_{I'}) \\ ({}^G\tilde{\mathbf{R}}_{I'}^\top {}^O\mathbf{R}_I^\top \mathbf{e}_3)^\top ({}^L\hat{\mathbf{R}}_{G_k}^\top {}^L\hat{\mathbf{R}}_{I_k} {}^O\mathbf{R}_I^\top \mathbf{e}_3) \end{bmatrix} + \mathbf{n}_{p_k} \quad (26)$$

where  $\tilde{\mathbf{y}}_{p_k} = [0 \ 1]^\top$ ,  $\mathbf{e}_3 = [0 \ 0 \ 1]^\top$ , and the Gaussian noise  $\mathbf{n}_{p_k} \sim \mathcal{N}(\mathbf{0}_{2 \times 1}, \Sigma_{p_k})$ .

With (26), we can derive the linearized error function as:

$$\mathbf{z}_{p_k} = \tilde{\mathbf{y}}_{p_k} - \hat{\mathbf{y}}_{p_k} \approx \mathbf{H}_{p_k} \boldsymbol{\xi}_k + \mathbf{n}_{p_k} \quad (27)$$

where the Jacobian matrix  $\mathbf{H}_{p_k} \triangleq \frac{\partial \mathbf{z}_{p_k}}{\partial \boldsymbol{\xi}_k} \in \mathbb{R}^{2 \times (21+6c+3K)}$ . More details are provided in the supplementary material.

## VI. INITIALIZATION

Accurate initial estimates are essential for estimator convergence. However, in the absence of manual intervention or GNSS, the initialization is restricted to rely solely on visual perception and the streetlight map, making it an extremely challenging task. Hence, we design an initialization module to efficiently estimate the initial relative transformation between the map frame and the local frame at system startup. For robust initialization, at least six streetlight detections are required. As shown in Fig. 7, the initialization is conducted in a divide-and-conquer manner with the following three steps.

**Map Division.** Leveraging the sparsity of the streetlight map, we extract all the triplets of streetlights, thus transforming the initialization problem into determining the optimal P3P solution [45]. However, given  $M$  streetlight clusters and  $N$  detections, the number of possible triplet matches is  $C_N^3 A_M^3$ , making it impractical to traverse them all. Fortunately, the hidden traversable area information in prior poses prompts a reasonable division of streetlight map. We sample the prior poses at intervals of  $\rho$  meters, with each pose corresponding to a circular region with radius  $\rho$ . This sampling reduces the total number of triplet matches to  $C_N^3 \sum_{r=1}^R A_{M_r}^3$ , where  $M_r$  is the number of streetlights within the  $r$ -th region. Additionally, the division strategy enables parallel computation, which further accelerates the iteration through triplet matches.

**Triplet Match Traversing.** Each triplet match is processed via the P3P algorithm [45] to derive a pose solution in  $SE(3)$ . Unreasonable solutions are discarded if the pose estimation deviates largely from the nearest prior pose in  $z$ -axis.

**Optimal Solution Selection.** For the remaining solutions, we design a two-level optimal solution selection method. In the first level, we use the solutions to find the matches of unselected streetlight detections. Given  $n_0$  unmatched detections and  $m_0$  unmatched streetlight clusters in a region, each potential match is scored using the sine of angle error in (22). We use the Hungarian algorithm [95] for the optimization:

$$\tilde{\mathcal{D}}_0^* = \arg \min_{\tilde{\mathcal{D}}_0} \sum_{d=1}^{n_0} \sum_{g=1}^{m_0+n_0} l_{dg} r_{a,dg}, \text{ s.t. } \sum_{d=1}^{n_0} l_{dg} \leq 1, \sum_{g=1}^{m_0+n_0} l_{dg} = 1.$$

The optimal matches for the detections can be identified. To better distinguish the quality of different solutions, we calculate the total reprojection error in (20) across all matches as the punishment score  $s_1$ . The top- $p$  solutions with the lowest scores in each region are then selected.

In the second level, we lower the threshold for binary-based streetlight detection. This adjustment increases the number of detections, but also introduces more noise from non-streetlight light sources. Each detection box is associated with the nearest projected streetlight cluster and the distance is used to calculate a reward score according to (19). Let  $s_2$  denote the summation of all rewards. The total score in the second level for each solution is given by  $s = -s_1 + \gamma s_2$ , where  $\gamma$  is a preset weight. The solution with the highest score  $s$  is set to the initial estimate of the relative transformation.

## VII. TRACKING RECOVERY

In the map regions with sparsely distributed streetlights, the robot may experience extended periods without streetlight detections. The accumulated pose drift over time makes it difficult to identify the correct matches for new streetlight detections, potentially resulting in tracking failures. To improve robustness, a tracking recovery module is proposed [46].

When the robot travels for a distance without matching streetlight detections, the tracking is considered lost, and the tracking recovery module is triggered. The limited number of streetlight detections makes it computationally feasible to employ the brute-force method to enumerate all possible streetlight match combinations. To select the optimal match,

we harness the key insight that incorrect match combinations result in increasing deviations of the estimated trajectories from the true values, whereas the correct match combination effectively minimizes pose drifts. Specifically, the state is cloned multiple times, with each copy being updated according to the corresponding match combination. The states with poses that deviate a lot from the nearest prior poses in the  $z$ -axis are discarded. All the remaining states will be propagated and updated in parallel until the traveled distance exceeds the set threshold and at least two streetlights are detected. During this process, incorrect match combinations exacerbate state errors, whereas correct matches constrain pose drifts, leading to significant differences in reprojection errors. We then re-adopt the two-level scoring strategy in the initialization module to identify the optimal state. The optimal state is regarded as the recovered state, indicating that the state is successfully corrected and ensuring the estimated trajectory continuity.

### VIII. FEATURE-DECOUPLED MSC-INEKF

Most InEKF-based VIO systems [84] [97] [98] maintain the positions of visual features within the body navigation state to form the  $SE_{2+K}(3)$  group. However, this feature-coupled approach results in the state transition matrix containing feature-related elements, which increases computational costs during propagation [88]. Herein, we analyze the prevalent feature-coupled MSC-InEKF, termed MSC-InEKF-FC. Following an in-depth theoretical analysis of multiple solutions, we propose a novel feature-decoupled MSC-InEKF that significantly improves efficiency without sacrificing accuracy.

#### A. MSC-InEKF-FC

For MSC-InEKF-FC, the feature positions are associated with the body navigation state to form the  $SE_{2+K}(3)$  group. In the system state,  $\mathbf{B}_k$  and  $\mathbf{X}_{G_k}$  remain unchanged as in (4), while  $\mathbf{X}_{I_k}$  and  $\mathbf{X}_{G_k}$  are modified as:

$$\mathbf{X}_{I_k} = \begin{bmatrix} {}^L\mathbf{R}_{I_k} & {}^L\mathbf{p}_{I_k} & {}^L\mathbf{v}_{I_k} & {}^L\mathbf{p}_{f_k} \\ \mathbf{0}_{3 \times 3} & \mathbf{I}_{3 \times 3} & \mathbf{0}_{3 \times 3} & \mathbf{0}_{3 \times 3} \end{bmatrix}, \mathbf{X}_{G_k} = \begin{bmatrix} {}^L\mathbf{R}_{G_k} & {}^L\mathbf{p}_{G_k} \\ \mathbf{0}_{1 \times 3} & 1 \end{bmatrix}. \quad (28)$$

All the error states remain unchanged except for the feature error state, which is reformulated as:

$${}^L\mathbf{p}_{f_k} = \text{Exp}(\boldsymbol{\xi}_{R_{LI_k}}) {}^L\hat{\mathbf{p}}_{I_k} + \mathbf{J}_I(\boldsymbol{\xi}_{R_{LI_k}}) \boldsymbol{\xi}_{p_{Lf_k}}. \quad (29)$$

Following similar procedures in Section IV-A, the state transition matrix and the noise Jacobian matrix are formulated as:

$$\Phi_i^{i+1} = \begin{bmatrix} \Phi_{II} & \Phi_{IB} & \mathbf{0}_{9 \times 6c} & \mathbf{0}_{9 \times 6} & \mathbf{0}_{9 \times 3} \\ \mathbf{0}_{6 \times 9} & \mathbf{I}_{6 \times 6} & \mathbf{0}_{6 \times 6c} & \mathbf{0}_{6 \times 6} & \mathbf{0}_{6 \times 3} \\ \mathbf{0}_{6c \times 9} & \mathbf{0}_{6c \times 6} & \mathbf{I}_{6c \times 6c} & \mathbf{0}_{6c \times 6} & \mathbf{0}_{6c \times 3} \\ \mathbf{0}_{6 \times 9} & \mathbf{0}_{6 \times 6} & \mathbf{0}_{6 \times 6c} & \mathbf{I}_{6 \times 6} & \mathbf{0}_{6 \times 3} \\ \mathbf{0}_{3 \times 9} & \Phi_{fB} & \mathbf{0}_{3 \times 6c} & \mathbf{0}_{3 \times 6} & \mathbf{I}_{3 \times 3} \end{bmatrix}, \mathbf{G}_i = \begin{bmatrix} \mathbf{G}_{II} & \mathbf{0}_{9 \times 6} \\ \mathbf{0}_{6 \times 6} & \mathbf{I}_{6 \times 6} \delta t \\ \mathbf{0}_{6c \times 6} & \mathbf{0}_{6c \times 6} \\ \mathbf{0}_{6 \times 6} & \mathbf{0}_{6 \times 6} \\ \mathbf{G}_{fI} & \mathbf{0}_{3 \times 6} \end{bmatrix}$$

where the block components  $\Phi_{II}$ ,  $\Phi_{IB}$ , and  $\mathbf{G}_{II}$  have the same formulations with (9).  $\Phi_{fB}$  and  $\mathbf{G}_{fI}$  are derived as:

$$\Phi_{fB} = \mathbf{G}_{fI} = [-({}^L\hat{\mathbf{p}}_{i+1})_{\times} \Delta \mathbf{R} \mathbf{J} \quad \mathbf{0}_{3 \times 3}]. \quad (30)$$

Notably,  $\Phi_{fB}$  causes an extra calculation in covariance propagation. Given  $K$  features, the covariance propagation requires a computation of  $O(K^2)$  flops. Compared to MSCKF which

only requires a level of about  $O(K)$  [88], the MSC-InEKF-FC process slows considerably when the number of features is large. The underlying reason is that the features are associated with the body navigation state, thus the state transition matrix is correlated with the features through (29).

#### B. MSC-InEKF-FDN

A naive feature-decoupled method (termed MSC-InEKF-FDN) represents the features in  $\mathbb{R}^3$  space, without maintaining them in any Lie group. In this way, only the relative transformation in  $\mathbf{X}_{G_k}$  is changed as following:

$$\mathbf{X}_{G_k} = \begin{bmatrix} {}^L\mathbf{R}_{G_k} & {}^L\mathbf{p}_{G_k} \\ \mathbf{0}_{1 \times 3} & 1 \end{bmatrix}. \quad (31)$$

The error state of the feature is formulated as:

$${}^L\mathbf{p}_{f_k} = {}^L\hat{\mathbf{p}}_{f_k} + \boldsymbol{\xi}_{p_{Lf_k}}. \quad (32)$$

The state transition matrix and the noise Jacobian matrix share the same formulation as (8). Although MSC-InEKF-FDN decouples the feature position states, the observability analysis reveals that it suffers from the inconsistency issue, introducing spurious information to state estimation. We first present the inherent unobservable dimensions of the system. The local frame aligns with gravity. When applying a 4-DoF transformation (three for translation and one for rotation around the gravity) to the local frame, the relative pose from frame  $I$  to  $G$  is not affected. Therefore, the observations provided by prior poses and streetlight clusters remain unchanged. Similar to visual-inertial SLAM systems, the observations of features and velocity are also not affected [97]. In summary, the dimension of the unobservable subspace is 4.

The observability matrix of the system is:

$$\mathcal{O} = [\mathcal{O}_0^\top \mathcal{O}_1^\top \dots \mathcal{O}_k^\top]^\top = [\mathbf{H}_0^\top \Phi_0^\top \mathbf{H}_1^\top \dots \Phi_0^{k^\top} \mathbf{H}_k^\top]^\top \quad (33)$$

where  $\mathbf{H}_k = [\mathbf{H}_{o_k}^\top \mathbf{H}_{f_k}^\top \mathbf{H}_{s_k}^\top \mathbf{H}_{p_k}^\top]^\top$ . For simplicity, we do not include the biases in the state vector as they are proved to be observable [99] for general motions. In addition, both MSC-InEKF and InEKF are derived based on the same propagation model and linearized error models with only the observation Jacobians calculated using different estimates [99]. Therefore, it is equivalent to the InEKF observability analysis, as long as we adjust the linearization points. The final considered state for MSC-InEKF-FDN is given by  $\mathbf{X}_k = (\mathbf{X}_{I_k}, \mathbf{X}_{G_k}, {}^L\mathbf{p}_{f_k})$ . Then, the right null space  $\mathcal{N}_N$  is:

$$\mathcal{N}_N = \begin{bmatrix} \mathbf{g}^\top & \mathbf{0}_{1 \times 3} & \mathbf{0}_{1 \times 3} & \mathbf{0}_{1 \times 3} & \mathbf{0}_{1 \times 3} & \mathbf{g}^\top ({}^L\hat{\mathbf{p}}_{f_k})_{\times} \\ \mathbf{0}_{3 \times 3} & \mathbf{I}_{3 \times 3} & \mathbf{0}_{3 \times 3} & \mathbf{0}_{3 \times 3} & \mathbf{I}_{3 \times 3} & \mathbf{I}_{3 \times 3} \end{bmatrix}^\top. \quad (34)$$

It shows that the unobservable subspace is affected by the feature estimate  ${}^L\hat{\mathbf{p}}_{f_k}$ , which causes an inconsistency problem.

#### C. MSC-InEKF-FDR

Another feature-decoupled method associates the feature with the relative transformation in  $\mathbf{X}_{G_k}$  to form  $SE_{1+K}(3)$ . Notably, this method is natural, since both the feature position state and the relative transformation state exhibit identical dynamics, characterized by stable states with zero velocities. We



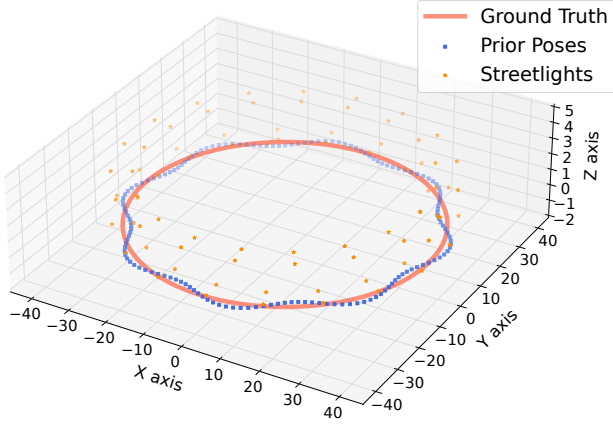


Fig. 8: The data used in the simulation. The pink trajectory is the ground-truth trajectory. The blue squares are prior poses generated in the mapping process and the orange stars represent the streetlights.

term it as MSC-InEKF-FDR. The state definition, propagation, and update are provided in the previous sections. The right null space of the observability matrix is spanned by:

$$\mathcal{N}_{R_1} = \begin{bmatrix} \mathbf{g}^\top & \mathbf{0}_{1 \times 3} & \mathbf{0}_{1 \times 3} & \mathbf{g}^\top & \mathbf{0}_{1 \times 3} & \mathbf{0}_{1 \times 3} \\ \mathbf{0}_{3 \times 3} & \mathbf{I}_{3 \times 3} & \mathbf{0}_{3 \times 3} & \mathbf{0}_{3 \times 3} & \mathbf{I}_{3 \times 3} & \mathbf{0}_{3 \times 3} \end{bmatrix}^\top. \quad (35)$$

Unlike MSC-InEKF-FDN, the unobservable subspace of MSC-InEKF-FDR is not affected by the state estimate, thus ensuring the consistency of the system. However, when the map-based information (i.e., streetlights and prior poses) is not available, the unobservable subspace of the system is:

$$\mathcal{N}_{R_2} = \begin{bmatrix} \mathbf{g}^\top & \mathbf{0}_{1 \times 3} & \mathbf{0}_{1 \times 3} & \mathbf{g}^\top & \mathbf{0}_{1 \times 3} & \mathbf{0}_{1 \times 3} \\ \mathbf{0}_{3 \times 3} & \mathbf{I}_{3 \times 3} & \mathbf{0}_{3 \times 3} & \mathbf{0}_{3 \times 3} & \mathbf{0}_{3 \times 3} & \mathbf{I}_{3 \times 3} \\ \mathbf{0}_{3 \times 3} & \mathbf{0}_{3 \times 3} & \mathbf{0}_{3 \times 3} & \mathbf{0}_{3 \times 3} & \mathbf{I}_{3 \times 3} & \mathbf{0}_{3 \times 3} \\ \mathbf{0}_{3 \times 3} & \mathbf{0}_{3 \times 3} & \mathbf{0}_{3 \times 3} & \mathbf{0}_{3 \times 3} & \mathbf{0}_{3 \times 3} & \mathbf{I}_{3 \times 3} \end{bmatrix}^\top. \quad (36)$$

The lack of streetlight observations and prior poses results in insufficient constraints on the relative transformation, thus the dimension of unobservable subspace should be 10. However, the existence of  ${}^L\hat{\mathbf{p}}_{f_k}$  leads to inconsistency.

#### D. MSC-InEKF-FDRC

Based on MSC-InEKF-FDR, we propose MSC-InEKF-FDRC that changes the feature association to the closest cloned pose  $\mathbf{X}_{CP_{k_k}}$  when no streetlight match is obtained. Therefore, the definitions of  $\mathbf{X}_{CP_{k_k}}$  and  $\mathbf{X}_{G_k}$  are updated as:

$$\mathbf{X}_{CP_{k_k}} = \begin{bmatrix} {}^L\mathbf{R}_{I_{k_k}} & {}^L\mathbf{p}_{I_{k_k}} & {}^L\mathbf{p}_{f_k} \\ \mathbf{0}_{2 \times 3} & \mathbf{I}_{2 \times 2} & \mathbf{0} \end{bmatrix}, \mathbf{X}_{G_k} = \begin{bmatrix} {}^L\mathbf{R}_{G_k} & {}^L\mathbf{p}_{G_k} \\ \mathbf{0}_{1 \times 3} & 1 \end{bmatrix}.$$

The formulation of other states is the same as (4). The error state of the feature is then changed to:

$${}^L\mathbf{p}_{f_k} = \text{Exp}(\boldsymbol{\xi}_{R_{CP_{k_k}}}) {}^L\hat{\mathbf{p}}_{f_k} + \mathbf{J}_l(\boldsymbol{\xi}_{R_{CP_{k_k}}}) \boldsymbol{\xi}_{p_{L_{f_k}}}. \quad (37)$$

The change in the representation of the feature error state results in the modification of the covariance. By denoting the state before the change with subscript 0 and the state after the change with subscript 1, we have:

$$\begin{aligned} {}^L\mathbf{p}_f &= \text{Exp}(\boldsymbol{\xi}_{R_0}) {}^L\hat{\mathbf{p}}_{f_0} + \mathbf{J}_l(\boldsymbol{\xi}_{R_0}) \boldsymbol{\xi}_{p_{L_{f_0}}} \\ {}^L\mathbf{p}_f &= \text{Exp}(\boldsymbol{\xi}_{R_1}) {}^L\hat{\mathbf{p}}_{f_1} + \mathbf{J}_l(\boldsymbol{\xi}_{R_1}) \boldsymbol{\xi}_{p_{L_{f_1}}}. \end{aligned} \quad (38)$$

TABLE I: The Noise Standard Deviation in the Simulation

Type	Measurement	Noise Standard Deviation
IMU	Angular Velocity	0.001 rad/s
	Specific Force	0.02 m/s <sup>2</sup>
	Gyroscope Bias	0.001 rad/s <sup>2</sup>
	Accelerometer Bias	0.001 m/s <sup>3</sup>
Odometer	Velocity	0.01 m/s
Camera	Image Features	1.0 pixel
	Streetlight Observations	1.0 pixel
Prior Pose	Rotation/Position	0.02 rad/0.02 m
Initial Relative Pose	Rotation/Position	0.04 rad/0.1 m

The feature state estimate remains unchanged, i.e.,  ${}^L\hat{\mathbf{p}}_f \triangleq {}^L\hat{\mathbf{p}}_{f_0} = {}^L\hat{\mathbf{p}}_{f_1}$ , hence the new feature error state is:

$$\boldsymbol{\xi}_{p_{L_{f_1}}} \approx -({}^L\hat{\mathbf{p}}_f) \times \boldsymbol{\xi}_{R_0} + ({}^L\hat{\mathbf{p}}_f) \times \boldsymbol{\xi}_{R_1} + \boldsymbol{\xi}_{p_{L_{f_0}}}. \quad (39)$$

The new covariance is then updated with (39). For the new association way, the right null space is formulated as:

$$\mathcal{N}_C = \begin{bmatrix} \mathbf{g}^\top & \mathbf{0}_{1 \times 3} & \mathbf{0}_{1 \times 3} & \mathbf{0}_{1 \times 3} & \mathbf{0}_{1 \times 3} & \mathbf{0}_{1 \times 3} \\ \mathbf{0}_{3 \times 3} & \mathbf{I}_{3 \times 3} & \mathbf{0}_{3 \times 3} & \mathbf{0}_{3 \times 3} & \mathbf{0}_{3 \times 3} & \mathbf{I}_{3 \times 3} \\ \mathbf{0}_{3 \times 3} & \mathbf{0}_{3 \times 3} & \mathbf{0}_{3 \times 3} & \mathbf{I}_{3 \times 3} & \mathbf{0}_{3 \times 3} & \mathbf{0}_{3 \times 3} \\ \mathbf{0}_{3 \times 3} & \mathbf{0}_{3 \times 3} & \mathbf{0}_{3 \times 3} & \mathbf{0}_{3 \times 3} & \mathbf{I}_{3 \times 3} & \mathbf{0}_{3 \times 3} \end{bmatrix}^\top. \quad (40)$$

Once the pose clone is marginalized, the features must change the associated pose clone. According to (39), the association change also involves a covariance update. If the sliding window size is small, the frequent covariance update can lead to an increased computation cost. To mitigate this issue, the features are re-associated with the relative transformation in  $\mathbf{X}_{G_k}$  when streetlight matches are available, as described in Section VIII-C. This strategy improves efficiency and avoids the inconsistency problem in (36). Further details of these filter representation variants are in the supplementary material.

## IX. EXPERIMENTAL RESULT

We conduct comprehensive experiments on the simulation, public dataset sequences, and the real-world collected dataset to thoroughly evaluate the proposed framework.

### A. Evaluation Metric

We utilize the Absolute Trajectory Error (ATE) to measure the localization accuracy, the Relative Trajectory Error (RPE) to reflect the pose drift, and the Normalized Estimation Error Squared (NEES) to evaluate the consistency [2]. For NEES, the value should be close to 1.0 if the system is consistent.

### B. Simulation Experiment

We perform simulation experiments to compare the proposed MSC-InEKF-FDRC with MSCKF, MSC-InEKF-FDC, MSC-InEKF-FDN, and MSC-InEKF-FDR in terms of accuracy, consistency, and efficiency. In the simulation, the shape of the ground truth trajectory in localization is a circle (the

TABLE II: ATE Results for Translation (m)/Rotation ( $^\circ$ ) of Different Algorithms in the Simulation Experiment

Algorithm/Result	Loc-traj	Rel-trans	Map-traj
MSCKF	0.44/0.36	<b>0.02/0.07</b>	0.44/0.40
MSC-InEKF-FC	<b>0.25/0.15</b>	<b>0.02/0.05</b>	<b>0.26/0.17</b>
MSC-InEKF-FDN	0.45/0.40	<b>0.02/0.05</b>	0.45/0.38
MSC-InEKF-FDR	0.46/0.35	<b>0.02/0.05</b>	0.46/0.38
MSC-InEKF-FDRC	<b>0.25/0.15</b>	<b>0.02/0.05</b>	<b>0.26/0.17</b>

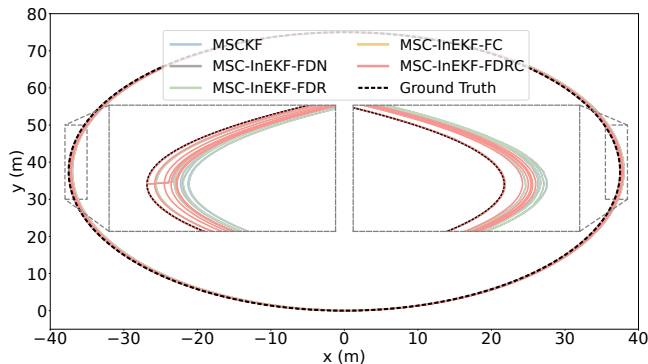


Fig. 9: Comparison of trajectories estimated by different algorithms.

pink trajectory in Fig. 8). The ground truth is then fed into the simulator of OpenVINS [2] to simulate the IMU, odometer, and feature point measurements. We also generate a mapping trajectory that is shaped like a wave swinging around the circle to simulate the prior poses (blue squares in Fig. 8). Points selected in the 3D space at a given interval are simulated as streetlights (orange stars in Fig. 8) so that the robot can observe 2 to 8 streetlights in each camera frame. The IMU, odometer, and visual data are generated, respectively, at 200, 10, and 25 Hz. All measurements are corrupted by additive Gaussian noises, as specified in Table I. The initial relative pose is given by adding Gaussian noises (Table I) to the true value. The robot runs ten times around the pink trajectory, and the total traveling distance is around 2513 m. In the ten loops, the streetlights and prior poses are only available in the first two and the last two loops, so the map information is absent for a long term (during the middle six loops).

**Evaluation of Accuracy.** We provide three different result types for comparison, namely the robot trajectory in the local reference frame (Loc-traj), the relative transformation between the local and the map frames (Rel-trans), and the trajectory in the map frame (Map-traj). Table II contains the ATE results for rotation and translation between different algorithms. As expected, MSC-InEKF-FDRC performs better than MSCKF because the combination of InEKF and MSCKF solves the inconsistency problem. Although MSC-InEKF-FDN and MSC-InEKF-FDR also combine InEKF with MSCKF, the inconsistency in feature association methods makes their performance not as accurate as MSC-InEKF-FDRC, and even worse than MSCKF in the translation part. It is not surprising that MSC-InEKF-FC achieves comparable accuracy with MSC-InEKF-FDRC as both their feature association ways preserve the correct observability. Moreover, it can be observed that all filters achieve competitive accuracy in Rel-trans. The reason

TABLE III: NEES Results for Translation/Rotation of Different Algorithms in the Simulation Experiment

Algorithm/Result	Loc-traj	Rel-trans	Map-traj
MSCKF	10.14/13.31	0.93/11.35	9.73/14.43
MSC-InEKF-FC	<b>1.29/1.92</b>	<b>0.94/1.34</b>	0.58/1.48
MSC-InEKF-FDN	7.63/16.15	<b>0.94/6.62</b>	7.50/12.89
MSC-InEKF-FDR	7.67/2.47	<b>0.94/1.34</b>	5.28/2.05
MSC-InEKF-FDRC	<b>1.29/1.92</b>	<b>0.94/1.34</b>	<b>0.59/1.48</b>

is that the map-based information (i.e., streetlights and prior poses) effectively bounds the drift of relative transformation while features and odometer measurements only constrain the local state. When map-based information is absent (i.e. during the middle 6 loops), the local trajectories drift, while the relative transformation is minimally affected. Fig. 9 visually compares the trajectories generated by different algorithms. The zoom-in areas show that the estimated trajectory of MSC-InEKF-FDRC (the pink one) is the closest to the ground truth.

**Evaluation of Consistency.** Table III includes the NEES results between different algorithms. Note that although the covariance of the pose in the map frame is not directly estimated, we do have the covariance of both  ${}^L\mathbf{T}_G$  and  ${}^L\mathbf{T}_I$ . Therefore, we can derive it using the relationship  ${}^G\mathbf{T}_I = {}^L\mathbf{T}_G^{-1}{}^L\mathbf{T}_I$ . Inflated NEES values are observed in MSCKF, MSC-InEKF-FDN, and MSC-InEKF-FDR, due to the underestimated state covariance caused by inconsistency. In contrast, MSC-InEKF-FC and MSC-InEKF-FDRC keep the correct dimension of the unobservable subspace, thus their NEES values are around 1, indicating consistent estimators. The qualitative results in Fig. 10 display the local-pose error with  $3\sigma$  bounds and the NEES variation of Loc-traj and Map-traj over time for different algorithms. The plots reveal that the estimation errors of MSC-InEKF-FDRC are well characterized in the uncertainty bounds. The NEES values for all filters initially remain at a low level owing to the map-based constraints. Subsequently, when the map information is absent, the MSC-InEKF-FDRC curve exhibits minor fluctuations, whereas the other curves increase rapidly, indicating the consistency of MSC-InEKF-FDRC.

**Evaluation of Efficiency.** The average runtime per step over the number of feature points is shown in Fig. 11, validating that MSC-InEKF-FC is time-consuming compared to other filters. For example, when the number of features increases to 50, the time consumption of MSC-InEKF-FC is approximately three times that of the others. Thanks to the decoupled feature association, the proposed MSC-InEKF-FDRC is much more time-saving and has efficiency similar to that of MSCKF.

Overall, the proposed MSC-InEKF-FDRC is an accurate, efficient, and consistent filter and representation design, playing a pivotal role within the nocturnal state estimation framework.

### C. Evaluation on the Public Dataset

**Setup.** There is a paucity of publicly available multi-sensor datasets for urban environments at night. Accordingly, we use the nighttime sequences from the public MCD dataset [100] to evaluate different algorithms. The MCD dataset consists of 18 sequences collected from 3 different campuses, including

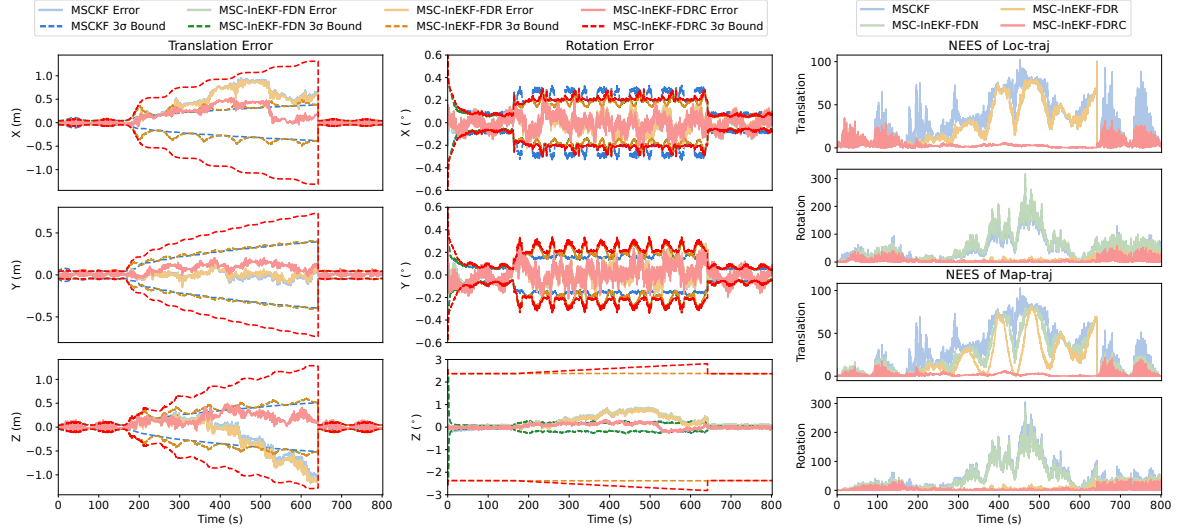


Fig. 10: Comparison of the estimation consistency. The left two columns show the local trajectory errors and the corresponding  $\pm 3\sigma$  bounds of different algorithms. The right column shows the NEES of local and map trajectories of different algorithms.

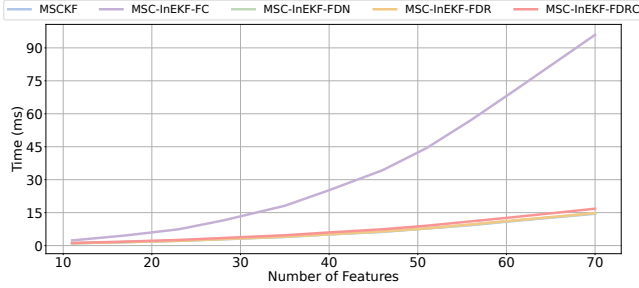


Fig. 11: Average runtime per step over the different number of feature points in the simulation.

3 sequences (*ntu\_night\_04*, *ntu\_night\_08*, and *ntu\_night\_13*) gathered by an all-terrain vehicle on campus NTU during the night. The character of the 3 sequences lies in the relatively rich illumination (Fig. 12). We leverage the images in these 3 sequences and the provided accurate survey-grade prior map to construct a streetlight map. The mapping process is similar to the description in Section V-A. The final streetlight map of the NTU campus is shown in the second image in Fig. 12. Since the odometer is not provided, we add noise to the interpolated velocity [2] to simulate the measurements.

**Result and Analysis.** For each sequence, we benchmark the proposed system without prior pose observations (Night-Voyager<sup>⊖</sup>), and compare the estimated trajectory in the map frame with those of state-of-the-art (SOTA) vision-aided state estimation methods augmented with odometer observations, including the odometer-aided VINS-Mono [3], [4] (VINS-Odom) and the odometer-aided OpenVINS [2] (OpenVINS-Odom). We also compare several popular visual localization algorithms which leverage different map types, including methods based on feature point maps (Hloc [32]), 3D line maps (VL-Line [56]), and point cloud maps (CMRNet [63] and LHMap [65]). For Hloc, SuperPoint [33] and SuperGlue [34] are utilized for feature map reconstruction and visual localization. Due to insufficient feature points at night, constructing a feature point map is challenging. Therefore, we use daytime sequences to build the map. In VL-Line, VINS-



Fig. 12: The prior map, the constructed streetlight map, and sampled images from the MCD dataset [100].

Mono [3] provides prior poses to identify line matches. For a fair comparison, we replace it with VINS-Odom. CMRNet and LHMap refine coarse poses with neural networks using images and projected point clouds as input. MSF is used to generate the coarse poses and integrate the refined poses. We select the *ntu\_night\_08* sequence for training the networks introduced in the aforementioned methods. Table IV reports the ATE results of different methods. Even without the assistance of prior pose observations, Night-Voyager<sup>⊖</sup> still significantly outperforms other algorithms in all sequences. The estimated trajectories are presented in Fig. 13. Thanks to the streetlight map, the trajectories estimated by Night-Voyager<sup>⊖</sup> align well with the ground truth. Nevertheless, although well-lit sequences promote the feature association, the estimated trajectories of VINS-Odom and OpenVINS-Odom inevitably suffer from pose drifts, indicating the critical role of object-level correspondences. Besides, 3D line maps have limited effectiveness in visual localization because a structured scene is required for VL-Line. However, the textural lines of traffic lanes and floor tile gaps, along with spurious line detections caused by uneven lighting, influence the line association. Essentially, the poor performance of VL-Line stems from the *insufficiency* and *inconsistency* issues of pixel-level features. Due to the limited information at night, the improvement of CMRNet and LHMap is much inferior to that of Night-Voyager, which demonstrates the substantial benefits brought by the object-level map and data association.

Ablation experiments are also performed. By replacing MSC-InEKF-FDRC with different filters, we obtain 4 versions of Night-Voyager<sup>⊖</sup>, namely MSCKF<sup>⊖</sup>, MSC-InEKF-



TABLE IV: ATE Results (m/ $^\circ$ ) on the MCD Dataset

Method/Sequence	<i>ntu_night_04</i> (1459 m)	<i>ntu_night_08</i> (2421 m)	<i>ntu_night_13</i> (1231 m)
OpenVINS-Odom	14.30/7.72	20.03/11.71	14.64/7.07
VINS-Odom	11.15/5.66	18.43/7.97	16.74/7.21
Hloc	—	—	—
VL-Line	10.34/4.73	21.44/5.85	11.27/13.28
CMRNet	26.67/11.21	#	20.25/9.07
LHMap	21.55/9.83	#	16.24/7.99
MSCKF $^\ominus$	0.81/1.20	40.87/12.39	6.28/4.48
MSC-InEKF-FC $^\ominus$	0.81/1.29	<b>0.25/0.80</b>	0.27/0.73
MSC-InEKF-FDN $^\ominus$	0.86/1.29	34.28/11.38	27.85/13.21
MSC-InEKF-FDR $^\ominus$	0.93/1.40	<b>x</b>	<b>0.24/0.71</b>
Night-Voyager $^\ominus$ w/o FP	0.86/ <b>1.15</b>	1.03/1.41	0.57/0.98
Night-Voyager $^\ominus$	<b>0.79/1.21</b>	<b>0.25/0.82</b>	0.27/0.73

— denotes that Hloc fails to construct the feature map.

# denotes the training sequence for CMRNet and LHMap.

**x** indicates the algorithm fails on the corresponding sequence.

The optimal results are highlighted in **bold**.

FC $^\ominus$ , MSC-InEKF-FDN $^\ominus$ , and MSC-InEKF-FDR $^\ominus$ . Consistent with the simulation results, the two Night-Voyager $^\ominus$  variants built on MSC-InEKF-FC and MSC-InEKF-FDR demonstrate the best results. In comparison, MSCKF $^\ominus$ , MSC-InEKF-FDN $^\ominus$ , and MSC-InEKF-FDR $^\ominus$  exhibit inferior performance. In *ntu\_night\_08*, there is a long distance with multiple false streetlight detections. Since the streetlight matching depends on the estimated pose, pose errors caused by inconsistency impact the results of data association, further exacerbating the errors. Consequently, MSCKF $^\ominus$ , MSC-InEKF-FDN $^\ominus$ , and MSC-InEKF-FDR $^\ominus$  fail to estimate the trajectory.

Furthermore, we analyze the role of feature points in nighttime localization. We record the ATE result of Night-Voyager $^\ominus$  without feature points (Night-Voyager $^\ominus$  w/o FP) in Table IV. The accuracy decreases without feature points, especially in *ntu\_night\_08*. Fig. 14 further presents the trajectory errors of both Night-Voyager $^\ominus$  and Night-Voyager $^\ominus$  w/o FP. Compared to Night-Voyager $^\ominus$ , Night-Voyager $^\ominus$  w/o FP has higher estimation errors, indicating the effectiveness of leveraging hybrid object-level and pixel-level features.

#### D. Evaluation on the Collected Dataset

**Setup.** In addition to evaluations on public datasets, further validation of the proposed framework is required through its deployment on real robots across diverse nocturnal urban scenarios. We utilize the wheeled robot equipped with multiple sensors for data collection. As Fig. 15 shows, the sensors consist of a front-facing RGB camera (30 Hz 1280 $\times$ 720 images), an odometer (10 Hz), and a Livox 360 $^\circ$  FoV LiDAR (10 Hz) integrating an ICM40609 IMU (200 Hz). Only IMU, odometer, and monocular camera measurements are used for nocturnal state estimation. The camera's intrinsics and all extrinsics among sensors are pre-calibrated, and the trajectory ground truth is provided by RTK GNSS sensors. To comprehensively evaluate the proposed framework, we collect nighttime data

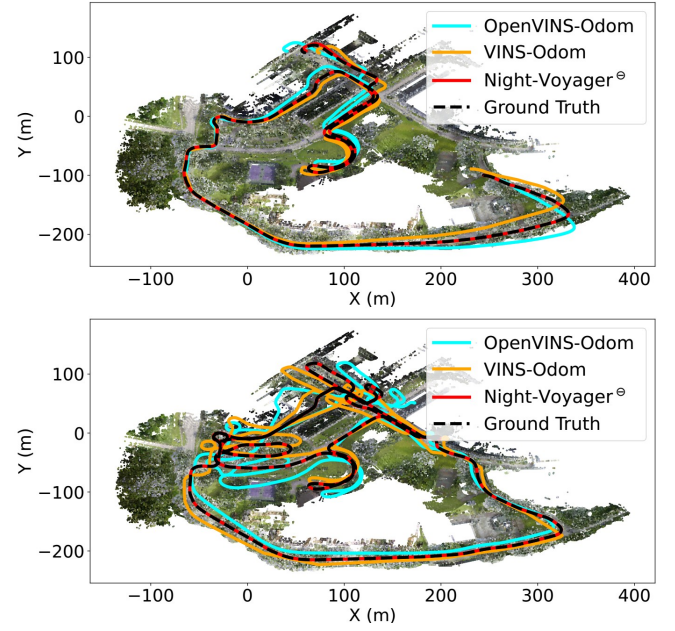


Fig. 13: Estimated trajectories of different algorithms on the prior map. Top: *ntu\_night\_04*. Bottom: *ntu\_night\_08*.

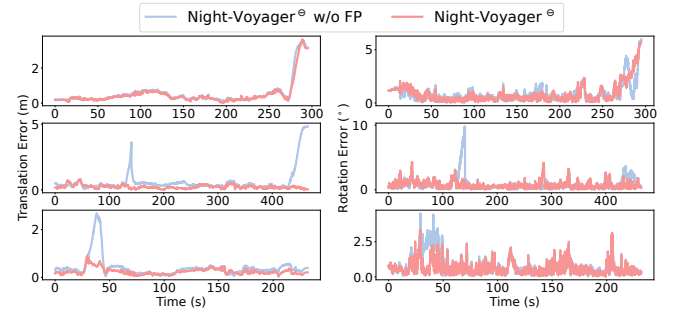


Fig. 14: Comparison of translation and rotation errors between the Night-Voyager $^\ominus$  with and without feature points. Top: *ntu\_night\_04*. Middle: *ntu\_night\_08*. Bottom: *ntu\_night\_13*.

from ten different scenes. Each scenario in the collected dataset comprises two sets: one for constructing the streetlight map and the other for validating nocturnal state estimation algorithms. The trajectories of these two sets are different and have distinct starting points. The dataset focuses on areas such as campuses, alleys, streets, and gardens, and exhibits poorer lighting conditions compared to the MCD dataset. Table V summarizes the characters of each sequence, including the distance, the scene type, and the distribution density of streetlights (a mixed distribution indicates the existence of both sparse and dense streetlight areas). Fig. 15 shows the example images and streetlight maps.

We utilize the YOLOv7 series [89] as the streetlight detector due to its high accuracy and real-time performance. About 3000 images labeled from different nighttime scenes are used to train the detection network. A desktop computer with an Intel i9-10900X CPU and an NVIDIA GeForce RTX 3090 GPU is used for network training, while all evaluation experiments are performed on an Intel NUC with an i7-1165G7 CPU. For all data-driven methods (i.e., Hloc [32], VL-Line [56], CMRNet [63], and LHMap [65]), except for Hloc, which is trained using additional mapping sequences collected during

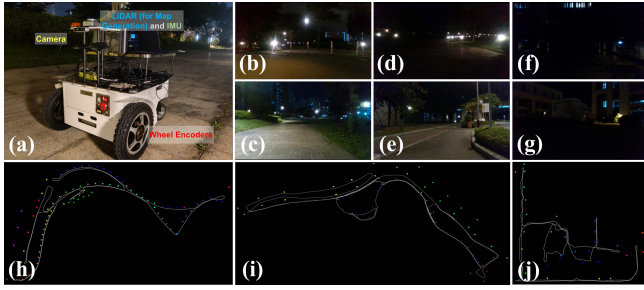


Fig. 15: The robot for data collection and the sequence examples. (a) displays the sensors on the robot. (b), (c), (d), (e), (f), and (g) are sampled images from the collected dataset. (h), (i), and (j) are the constructed streetlight maps of *Scene\_02*, *Scene\_03*, and *Scene\_04*.

the daytime, the networks are trained with nighttime mapping sequences. These four methods are trained and evaluated on the aforementioned desktop computer.

**Evaluation and Analysis.** In the collected dataset, we compare Night-Voyager with the aforementioned methods and the previous work, Night-Rider [46]. The quantitative results and estimated trajectories are shown in Table VI and Fig. 17. Contrary to the results observed in the brighter scenarios of the MCD dataset, both OpenVINS-Odom and VINS-Odom perform significantly worse in the darker scenarios of the collected dataset, due to the limited tracked features under unfavorable lighting conditions. As shown in Fig. 16, the performance of Hloc is significantly affected by the severe illumination differences between daytime and nighttime images. VL-Line, CMRNet, and LHMap also perform poorly in dark environments. Hloc even fails across all sequences, poor lighting conditions pose challenges in identifying reliable matches between images and feature maps. In contrast, Night-Voyager has a much smaller trajectory error due to the streetlight map. Night-Rider shows significant performance variations across different sequences. Two reasons lead to its poor robustness: 1) Night-Rider leverages InEKF as the estimator. Compared to MSC-InEKF-FDRC, which utilizes historical information in the sliding window, InEKF emphasizes the current observation, making Night-Rider prone to failures when incorrect matches are determined. 2) Night-Rider is highly dependent on streetlights, causing poor robustness when no streetlight is visible. In Night-Voyager, all feature points, prior poses, and virtual centers serve as system observations. Therefore, regardless of the density of the streetlight distribution, Night-Voyager achieves remarkably accurate and robust localization in all scenes ( $<0.2\%$  relative error of the total trajectory).

We then conduct an ablation study to assess the impact of feature points, prior poses, and virtual centers. Four variants of the proposed algorithm are evaluated, including 1) MSF: Night-Voyager only fusing with the measurements of IMU, odometer, and feature points; 2) Night-Voyager w/o FP: Night-Voyager without utilizing feature points; 3) Night-Voyager w/o PP: Night-Voyager without utilizing prior poses; 4) Night-Voyager w/o VC: Night-Voyager utilizing the geometric centers of streetlight clusters instead of the virtual centers. In Table VI, the results of MSF and Night-Voyager verify the importance of the prior streetlight map. In addition, the proposed data association algorithm determines the correct streetlight

TABLE V: Details of the Collected Dataset

Seq.	Dist. (m)	Scene	Distrib.	Map Storage (MB)			
				St.	Line	PCD	Feat.
<i>Scene_01</i>	724	Avenue & Garden	Sparse	3.0	0.4	81.3	648.6
<i>Scene_02</i>	613	Lane	Dense	2.9	0.1	57.4	318.1
<i>Scene_03</i>	635	Lane & Pavement	Sparse	6.0	0.2	61.4	534.9
<i>Scene_04</i>	305	Garden	Sparse	3.3	0.3	58.4	577.4
<i>Scene_05</i>	777	Seaside Road	Dense	3.8	0.1	54.1	283.4
<i>Scene_06</i>	1071	Seaside Road	Dense	3.5	0.1	54.1	361.2
<i>Scene_07</i>	892	Avenue & Garden	Mixed	5.2	0.5	75.6	446.2
<i>Scene_08</i>	719	Alley & Campus	Mixed	4.5	0.2	71.6	621.4
<i>Scene_09</i>	842	Campus	Mixed	6.1	0.6	86.1	511.7
<i>Scene_10</i>	601	Bridge & Avenue	Mixed	2.9	0.6	112.0	446.2

Seq., Dist., and Distrib. are short for sequence, distance, and streetlight distribution. St., Line, PCD, and Feat. denote the streetlight map, the line map, the point-cloud map, and the feature-point map.

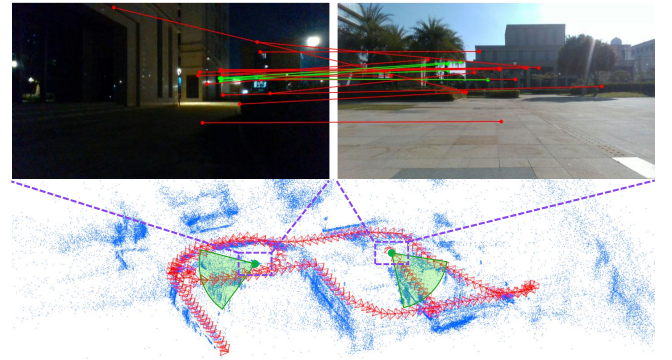


Fig. 16: Hloc failure case. Top left: captured image during nocturnal localization. Top right: queried image from the mapping sequence. Bottom: constructed feature map and mapping trajectory.

matches, thus the streetlight information is fully leveraged for nocturnal state estimation. When feature points are not utilized, there is almost no loss of accuracy in most sequences. This phenomenon is natural since it is difficult to perform feature tracking in scenes under poor lighting conditions. In most sequences, prior poses improve the performance of Night-Voyager, indicating that they can provide versatile information for estimation. We also observe that Night-Voyager achieves improvements in almost all sequences compared with Night-Voyager w/o VC. This is because virtual centers mitigate the inconsistency between the light bulb center and the geometric center of the streetlight cluster, providing more accurate and physically plausible constraints for state update.

In Fig. 18, we give the RPE results of Night-Voyager w/o FP, Night-Voyager w/o PP, Night-Voyager w/o VC, and Night-Voyager to demonstrate the effect of feature points, prior poses, and virtual centers. Three different segment lengths (50 m, 100 m, and 200 m) are selected for statistical RPE analysis. In Fig. 18, the translation errors increase with the segment length, indicating the pose drift in nocturnal localization. By comparing the translation errors among Night-Voyager, Night-Voyager w/o PP, and Night-Voyager w/o VC, we can see that the drift in most sequences is alleviated, which further proves the effectiveness of prior poses and virtual centers.

TABLE VI: ATE results (m/°) of Different Algorithms on the Collected Dataset

Method/Sequence	Scene_01	Scene_02	Scene_03	Scene_04	Scene_05	Scene_06	Scene_07	Scene_08	Scene_09	Scene_10
OpenVINS-Odom	✗	39.44/56.31	✗	18.10/17.58	✗	✗	41.90/23.29	✗	✗	26.13/15.36
VINS-Odom	11.38/4.05	39.45/23.25	✗	7.17/13.23	✗	13.86/11.34	27.74/11.47	18.78/11.31	✗	✗
Hloc	✗	✗	✗	✗	✗	✗	✗	✗	✗	✗
VL-Line	7.27/3.56	17.02/18.94	✗	5.05/4.63	✗	9.33/5.03	21.86/19.16	18.80/24.65	✗	✗
CMRNet	25.58/9.29	41.04/37.11	✗	10.02/17.29	✗	✗	✗	28.56/16.22	20.61/11.53	✗
LHMap	20.11/15.12	40.92/36.50	✗	8.56/17.92	✗	20.54/13.93	✗	22.65/19.03	30.52/17.14	✗
Night-Rider	0.88/3.71	✗	4.26/5.42	0.36/1.86	0.33/1.67	0.38/ <b>0.56</b>	18.85/20.03	✗	✗	27.98/24.38
MSF	11.84/9.70	46.56/58.41	✗	8.21/28.11	✗	✗	✗	✗	✗	34.37/21.26
Night-Voyager w/o FP	0.20/ <b>0.57</b>	0.39/0.87	0.54/ <b>0.93</b>	0.27/0.88	<b>0.29/0.77</b>	0.38/ <b>0.56</b>	0.49/ <b>1.12</b>	<b>0.41/0.84</b>	0.55/0.83	<b>0.45/0.96</b>
Night-Voyager w/o PP	0.20/0.60	<b>0.31/0.83</b>	0.52/0.94	0.31/ <b>0.86</b>	0.30/0.78	<b>0.32/0.64</b>	0.49/1.13	0.43/ <b>0.84</b>	0.58/0.86	<b>0.45/0.96</b>
Night-Voyager w/o VC	0.20/0.60	0.57/1.00	0.54/0.99	0.29/1.06	0.34/0.94	0.37/0.64	0.48/1.15	0.46/0.96	0.61/0.93	0.46/0.97
Night-Voyager	<b>0.19/0.57</b>	0.38/0.87	<b>0.49/0.93</b>	<b>0.26/0.90</b>	<b>0.29/0.78</b>	0.38/ <b>0.56</b>	<b>0.44/1.12</b>	<b>0.41/0.84</b>	<b>0.54/0.80</b>	<b>0.45/0.96</b>

✗ indicates the algorithm fails to run the corresponding sequence. The optimal results are highlighted in **bold**.

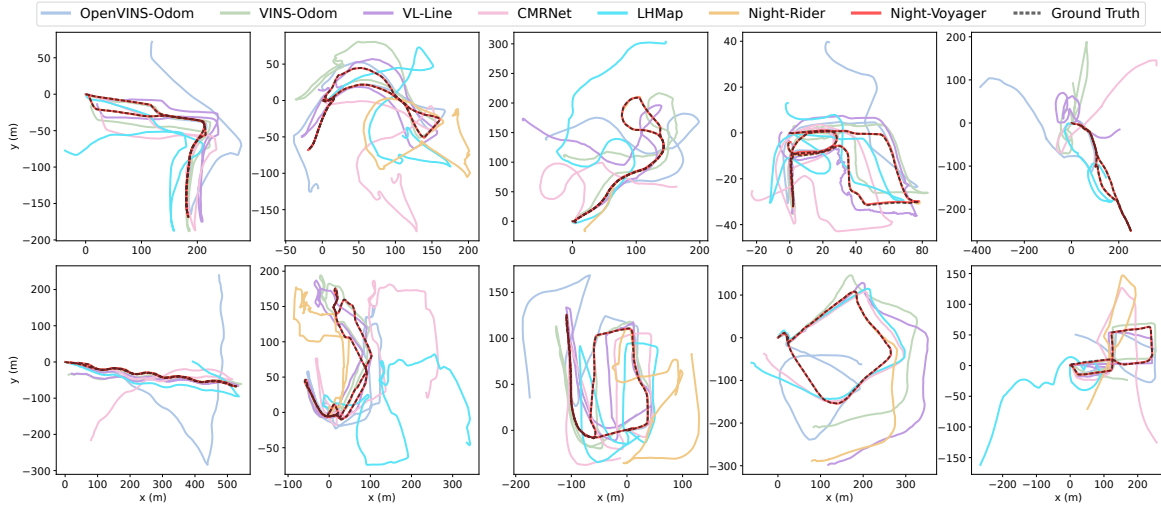


Fig. 17: Comparison of the estimated trajectories of different algorithms on the collected dataset. (a) Scene\_01. (b) Scene\_02. (c) Scene\_03. (d) Scene\_04. (e) Scene\_05. (f) Scene\_06. (g) Scene\_07. (h) Scene\_08. (i) Scene\_09. (j) Scene\_10.

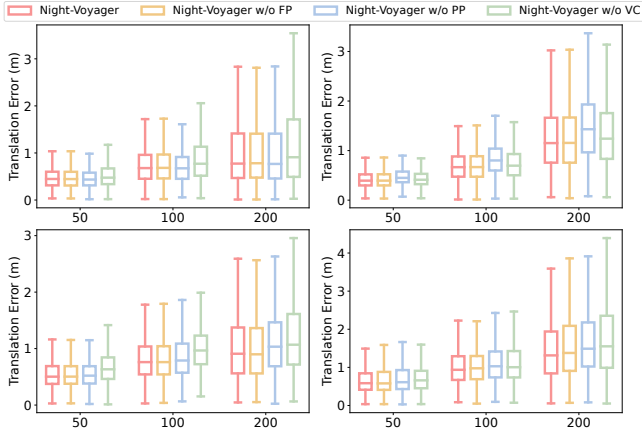


Fig. 18: Comparison of RPE results on different sequences. (a) Scene\_02. (b) Scene\_06. (c) Scene\_08. (d) Scene\_09.

### E. Evaluation of Initialization

From the mapping set of various scenes, we select images with at least six streetlight detection boxes and feed them into the initialization module to estimate the corresponding relative transformation. We gather the following statistics to evaluate the initialization module: 1) *Success Rate (SR)*: The ratio of the number of successful initializations to the total number of input images for each sequence. Initialization is considered successful when the Absolute Pose Error (APE) between the estimated relative pose and the true value is less than a set threshold (0.5 m for translation and 3° for rotation). 2) *Average Running Time (ART)*: The average running time of the initialization in different sequences. 3) *Average APE (AAPE)*: Average APE between the estimated relative pose and the true value of the successful initializations. The results are presented in Table VII.

In general, the proposed initialization module exhibits high



TABLE VII: SR (%), ART (s), and AAPE (m/°) of the Initialization Module on Different Sequences

Method	Metric	Scene_01	Scene_02	Scene_03	Scene_04	Scene_05	Scene_06	Scene_07	Scene_08	Scene_09	Scene_10
w/o Coarse Position	SR	81.3	79.2	100.0	100.0	58.9	60.9	75.0	100.0	100.0	81.6
	ART	2.47	5.38	0.76	0.69	4.82	1.76	6.49	5.72	2.11	6.11
	AAPE	0.25/0.40	0.18/0.51	0.32/1.66	0.31/0.28	0.24/0.74	0.21/0.63	0.25/0.34	0.35/0.74	0.34/0.45	0.25/0.57
w/ Coarse Position (10 m)	SR	88.9	94.2	100.0	100.0	85.7	87.8	81.8	100.0	100.0	90.0
	ART	0.27	0.50	0.09	0.11	0.51	0.18	0.35	0.47	0.13	0.41
	AAPE	0.25/0.48	0.20/0.64	0.32/1.66	0.31/0.28	0.27/0.70	0.22/0.57	0.23/0.31	0.35/0.74	0.34/0.45	0.25/0.55



Fig. 19: Examples of successful initialization (green outlines) and failed initialization (red outlines). The red dots in the images represent the projected streetlight points. The blue boxes are streetlight detections. The green numbers above detections indicate the indices of matched streetlight clusters (−1: no matched streetlight).

success rates, especially in scenarios with sparsely distributed streetlights. Fig. 19 shows some successful cases (figures with green outlines). We can see that the streetlight points (red dots) projected from the estimated relative poses all fall in the streetlight detection boxes (blue boxes), which proves the high accuracy of the relative pose estimation. We also observe that the initialization module is robust to incorrect streetlight detections (i.e., false detection or streetlights not constructed in the map). All incorrect detections are identified as unmatched streetlights (marked as −1). In sequences with a dense distribution of streetlights like *Scene\_02*, *Scene\_05*, and *Scene\_06*, the success rate obviously declines. The fourth column of Fig. 19 depicts two common failure cases to illustrate the reasons: 1) Overlapped streetlight detections. For densely distributed streetlights, the detection boxes are prone to overlap, resulting in a significant deviation of the box centers to the true coordinates. Therefore, the affected score in initialization leads to the selection of incorrect triplet matches. 2) Repetitive streetlight distribution patterns. In scenarios with a dense streetlight distribution, there is a higher likelihood of areas with similar streetlight distribution patterns, thus confusing the initialization module. The sector-shaped areas on the bottom right of Fig. 19 illustrate this situation. Erroneous initialization can lead to localization failures. To minimize the likelihood of this situation, we add an interface to the initialization module to receive a coarse initial position. When users provide this value, the module excludes solutions that are more than 10 m from the given position. Significant improvements can be seen in Table VII. The running time results are shown in Table VII. By utilizing prior poses for streetlight map division, the initialization module demonstrates commendable time efficiency, allowing the robot to quickly determine its pose within the map and execute tasks efficiently.

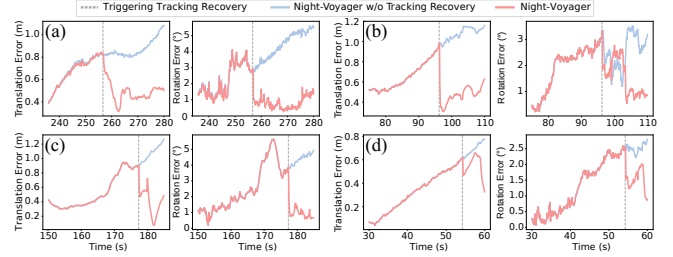


Fig. 20: Comparison of translation and rotation errors with and without the tracking recovery module on different sequences. (a) *Scene\_02*. (b) *Scene\_05*. (c) *Scene\_07*. (d) *Scene\_08*.

#### F. Evaluation of Tracking Recovery

To test the tracking recovery module, we randomly select segments (lasting 30 to 60 seconds) from the collected sequences, during which we turn off the data association module to test whether the tracking recovery module can correct pose drifts. The segments are chosen at moments when few streetlights are visible, effectively imitating scenarios of tracking loss. Table VIII presents the ATE results of Night-Voyager with and without the tracking recovery module. The results indicate that Night-Voyager without tracking recovery fails to correct the robot pose in most sequences. The failure significantly impacts localization, as large drifts lead to erroneous streetlight matches, thus further exacerbating errors. In contrast, the tracking recovery module enables rapid pose correction through the brute-force matching method and the scoring strategy, thereby mitigating potential accuracy loss. Fig. 20 visually displays the changes in translation and rotation errors between the two variants. When tracking recovery is triggered (gray dashed line), the pose errors decrease immediately. However, without tracking recovery, errors continue to increase, eventually leading to localization failures.

#### G. Running Time and Map Storage

Fig. 21 shows the time consumption of Night-Voyager on both the MCD and the collected datasets. Meanwhile, we compare the computation cost of the Night-Voyager variant which exploits MSC-InEKF-FC. For a fair comparison of estimators, the time spent on streetlight detection is excluded from the results. Compared to MSC-InEKF-FC, MSC-InEKF-FDRC (the default estimator of Night-Voyager, see Section VIII-D) is much more efficient in well-lit scenes, such as MCD sequences, confirming the efficiency of MSC-InEKF-FDRC. In the collected dataset, the runtime of MSC-InEKF-FC is slightly higher than that of MSC-InEKF-FDRC. The adverse lighting condition reduces the number of feature points, and

TABLE VIII: ATE Results (m/°) with and without the Tracking Recovery Module on Different Sequences

Method	Scene_01	Scene_02	Scene_03	Scene_04	Scene_05	Scene_06	Scene_07	Scene_08	Scene_09	Scene_10
Night-Voyager w/o TR	<b>0.20/0.56</b>	✗	✗	15.50/24.74	✗	✗	✗	✗	✗	✗
Night-Voyager	<b>0.20/0.56</b>	<b>0.39/0.88</b>	<b>0.61/1.06</b>	<b>0.32/1.08</b>	<b>0.30/0.89</b>	<b>0.39/0.57</b>	<b>0.51/1.20</b>	<b>0.50/1.16</b>	<b>0.55/1.05</b>	<b>0.45/0.96</b>

✗ indicates the algorithm fails on the corresponding sequence. The optimal results are highlighted in **bold**.

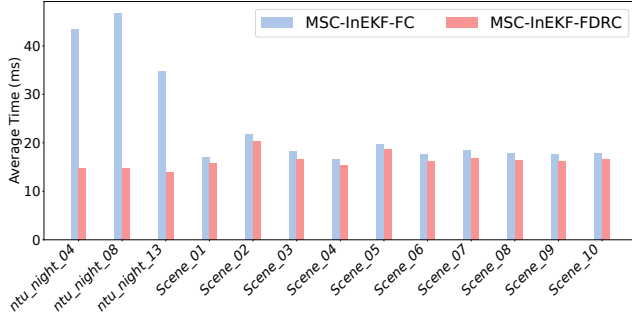


Fig. 21: Time consumption of MSC-InEKF-FC and MSC-InEKF-FDRC on both the MCD and the collected datasets.

thus the computation cost of MSC-InEKF-FC remains low. The map storage is also compared in Table V. The constructed streetlight maps are highly space-efficient and require significantly less storage than point-cloud maps or feature-point maps. In summary, Night-Voyager delivers accurate and real-time localization results at night with minimal storage requirements, independent of varying lighting conditions.

## X. CONCLUSION

In this work, we propose Night-Voyager, a consistent and efficient framework that harnesses rare object-level information from streetlight maps to fundamentally resolve the *insufficiency* and *inconsistency* bottlenecks inherent in nocturnal visual tasks. A fast global initialization is designed to precisely boot the system. Leveraging cross-modal correspondences, streetlight observations can provide accurate state updates. Additionally, pixel-level visual features endow Night-Voyager with the capability of all-day localization. With the feature-decoupled MSC-InEKF, Night-Voyager achieves consistent and efficient state estimation. Comprehensive simulation and real-world experiments demonstrate the efficacy, robustness, efficiency, and high accuracy of Night-Voyager.

This work reveals that conventional visual methods are prone to failure in low-light cases, even with active lighting or image enhancement. The genesis is the reliance on pixel-level correspondences. Unlike pixel-level features, object-level features are immune to inconsistency and transience encountered in tracking, leading to substantial accuracy improvements and a fundamental solution for nocturnal visual state estimation. While primarily designed for urban environments, Night-Voyager can be effectively deployed in other dark scenarios featuring stable light sources (e.g., factories, mines, parking lots, wharves, and tunnels). Significantly, this work reinforces a seminal insight that remains equally essential for both model-based and data-driven methodologies: Prior is all you need – whether from sensors, physical models, or learned models.

In future work, we aim to develop an all-day navigation framework, leveraging adaptive object-level perception approaches. Another promising direction is to design generalizable methods that integrate semantic information or object tracking to incorporate temporal constraints without relying on prior maps. Finally, an all-day visual place recognition model is also essential for robust long-term navigation.

## REFERENCES

- [1] F. Rubio, F. Valero, and C. Llopi-Albert, “A review of mobile robots: Concepts, methods, theoretical framework, and applications,” *International Journal of Advanced Robotic Systems*, vol. 16, no. 2, p. 1729881419839596, 2019. **1**
- [2] P. Geneva, K. Eickenhoff, W. Lee, Y. Yang, and G. Huang, “OpenVINS: A research platform for visual-inertial estimation,” in *2020 IEEE International Conference on Robotics and Automation (ICRA)*. IEEE, 2020, pp. 4666–4672. **1, 4, 11, 12, 13**
- [3] T. Qin, P. Li, and S. Shen, “VINS-mono: A robust and versatile monocular visual-inertial state estimator,” *IEEE Transactions on Robotics*, vol. 34, no. 4, pp. 1004–1020, 2018. **1, 4, 13**
- [4] J. Liu, W. Gao, and Z. Hu, “Visual-inertial odometry tightly coupled with wheel encoder adopting robust initialization and online extrinsic calibration,” in *2019 IEEE/RSJ International Conference on Intelligent Robots and Systems (IROS)*. IEEE, 2019, pp. 5391–5397. **1, 4, 13**
- [5] C. Forster, Z. Zhang, M. Gassner, M. Werlberger, and D. Scaramuzza, “Svo: Semidirect visual odometry for monocular and multicamera systems,” *IEEE Transactions on Robotics*, vol. 33, no. 2, pp. 249–265, 2016. **1, 4**
- [6] J. Engel, V. Koltun, and D. Cremers, “Direct sparse odometry,” *IEEE transactions on pattern analysis and machine intelligence*, vol. 40, no. 3, pp. 611–625, 2017. **1, 4**
- [7] R. Mur-Artal and J. D. Tardós, “Orb-slam2: An open-source slam system for monocular, stereo, and rgb-d cameras,” *IEEE transactions on robotics*, vol. 33, no. 5, pp. 1255–1262, 2017. **1, 4**
- [8] M. Bloesch, M. Burri, S. Omari, M. Hutter, and R. Siegwart, “Iterated extended kalman filter based visual-inertial odometry using direct photometric feedback,” *The International Journal of Robotics Research*, vol. 36, no. 10, pp. 1053–1072, 2017. **1, 4**
- [9] C. Campos, R. Elvira, J. J. G. Rodríguez, J. M. Montiel, and J. D. Tardós, “Orb-slam3: An accurate open-source library for visual, visual-inertial, and multimap slam,” *IEEE Transactions on Robotics*, vol. 37, no. 6, pp. 1874–1890, 2021. **1, 4**
- [10] J. Kim, Y. Cho, and A. Kim, “Proactive camera attribute control using bayesian optimization for illumination-resilient visual navigation,” *IEEE Transactions on Robotics*, vol. 36, no. 4, pp. 1256–1271, 2020. **2, 4**
- [11] J. Kim, M.-H. Jeon, Y. Cho, and A. Kim, “Dark synthetic vision: Lightweight active vision to navigate in the dark,” *IEEE Robotics and Automation Letters*, vol. 6, no. 1, pp. 143–150, 2020. **2, 4**
- [12] Y. Lin, S. Wang, Y. Jiang, and B. Han, “Breaking of brightness consistency in optical flow with a lightweight cnn network,” *IEEE Robotics and Automation Letters*, 2024. **2**
- [13] C. F. Bohren and D. R. Huffman, *Absorption and scattering of light by small particles*. John Wiley & Sons, 2008. **2**
- [14] C. Baron, *Adobe Photoshop Forensics: Sleuths, Truths, and Fauxtography*. Thomson Course Technology, 2008. [Online]. Available: <https://books.google.com/books?id=1c8LAAAQBAJ> **2**
- [15] T. Grimm and M. Grimm, *The Basic Book of Photography*, ser. Basic Book of Photography. Plume, 1997. [Online]. Available: <https://books.google.com/books?id=xIMrAQAAAJ> **2**
- [16] V. Blahnik, B. Voelker, C. Ag, V. Blahnik, and B. Voelker, “About the reduction of reflections for camera lenses how t\*-coating made glass invisible,” 2016. **2**

- [17] Z. Zhang, C. Forster, and D. Scaramuzza, "Active exposure control for robust visual odometry in hdr environments," in *2017 IEEE international conference on robotics and automation (ICRA)*. IEEE, 2017, pp. 3894–3901. 2, 4
- [18] N. Yang, R. Wang, X. Gao, and D. Cremers, "Challenges in monocular visual odometry: Photometric calibration, motion bias, and rolling shutter effect," *IEEE Robotics and Automation Letters*, vol. 3, no. 4, pp. 2878–2885, 2018. 2, 4
- [19] A. Yamasaki, H. Takauji, S. Kaneko, T. Kanade, and H. Ohki, "Denighting: Enhancement of nighttime images for a surveillance camera," in *2008 19th International Conference on Pattern Recognition*. IEEE, 2008, pp. 1–4. 2
- [20] X. Dong, Y. Pang, and J. Wen, "Fast efficient algorithm for enhancement of low lighting video," in *ACM SIGGRAPH 2010 posters*, 2010, pp. 1–1. 2
- [21] K. Fotiadou, G. Tsagakatakis, and P. Tsakalides, "Low light image enhancement via sparse representations," in *Image Analysis and Recognition: 11th International Conference, ICIAR 2014, Vilamoura, Portugal, October 22-24, 2014, Proceedings, Part I 11*. Springer, 2014, pp. 84–93. 2
- [22] K. G. Lore, A. Akintayo, and S. Sarkar, "Llnet: A deep autoencoder approach to natural low-light image enhancement," *Pattern Recognition*, vol. 61, pp. 650–662, 2017. 2, 4
- [23] Y. Jiang, X. Gong, D. Liu, Y. Cheng, C. Fang, X. Shen, J. Yang, P. Zhou, and Z. Wang, "Enlightengan: Deep light enhancement without paired supervision," *IEEE transactions on image processing*, vol. 30, pp. 2340–2349, 2021. 2, 4
- [24] L. Ma, T. Ma, R. Liu, X. Fan, and Z. Luo, "Toward fast, flexible, and robust low-light image enhancement," in *Proceedings of the IEEE/CVF conference on computer vision and pattern recognition*, 2022, pp. 5637–5646. 2, 4
- [25] S. Yang, M. Ding, Y. Wu, Z. Li, and J. Zhang, "Implicit neural representation for cooperative low-light image enhancement," in *Proceedings of the IEEE/CVF International Conference on Computer Vision*, 2023, pp. 12 918–12 927. 2, 4
- [26] Y. Wu, C. Pan, G. Wang, Y. Yang, J. Wei, C. Li, and H. T. Shen, "Learning semantic-aware knowledge guidance for low-light image enhancement," in *Proceedings of the IEEE/CVF Conference on Computer Vision and Pattern Recognition*, 2023, pp. 1662–1671. 2, 4
- [27] W. Wang, H. Yang, J. Fu, and J. Liu, "Zero-reference low-light enhancement via physical quadruple priors," in *Proceedings of the IEEE/CVF Conference on Computer Vision and Pattern Recognition*, 2024, pp. 26 057–26 066. 2, 4
- [28] D. G. Lowe, "Distinctive image features from scale-invariant keypoints," *International journal of computer vision*, vol. 60, pp. 91–110, 2004. 2
- [29] E. Rosten and T. Drummond, "Machine learning for high-speed corner detection," in *Computer Vision—ECCV 2006: 9th European Conference on Computer Vision, Graz, Austria, May 7-13, 2006. Proceedings, Part I 9*. Springer, 2006, pp. 430–443. 2
- [30] E. Rublee, V. Rabaud, K. Konolige, and G. Bradski, "Orb: An efficient alternative to sift or surf," in *2011 International conference on computer vision*. Ieee, 2011, pp. 2564–2571. 2
- [31] S. Leutenegger, M. Chli, and R. Y. Siegwart, "Brisk: Binary robust invariant scalable keypoints," in *2011 International conference on computer vision*. Ieee, 2011, pp. 2548–2555. 2
- [32] P.-E. Sarlin, C. Cadena, R. Siegwart, and M. Dymczyk, "From coarse to fine: Robust hierarchical localization at large scale," in *Proceedings of the IEEE/CVF conference on computer vision and pattern recognition*, 2019, pp. 12 716–12 725. 2, 13, 14
- [33] D. DeTone, T. Malisiewicz, and A. Rabinovich, "Superpoint: Self-supervised interest point detection and description," in *Proceedings of the IEEE conference on computer vision and pattern recognition workshops*, 2018, pp. 224–236. 2, 13
- [34] P.-E. Sarlin, D. DeTone, T. Malisiewicz, and A. Rabinovich, "Superglue: Learning feature matching with graph neural networks," in *Proceedings of the IEEE/CVF conference on computer vision and pattern recognition*, 2020, pp. 4938–4947. 2, 13
- [35] J. Sun, Z. Shen, Y. Wang, H. Bao, and X. Zhou, "Loftr: Detector-free local feature matching with transformers," in *Proceedings of the IEEE/CVF conference on computer vision and pattern recognition*, 2021, pp. 8922–8931. 2
- [36] J. Ma, X. Jiang, A. Fan, J. Jiang, and J. Yan, "Image matching from handcrafted to deep features: A survey," *International Journal of Computer Vision*, vol. 129, no. 1, pp. 23–79, 2021. 2
- [37] X. Jiang, J. Ma, G. Xiao, Z. Shao, and X. Guo, "A review of multimodal image matching: Methods and applications," *Information Fusion*, vol. 73, pp. 22–71, 2021. 2
- [38] W. Song, M. Suganuma, X. Liu, N. Shimobayashi, D. Maruta, and T. Okatani, "Matching in the dark: A dataset for matching image pairs of low-light scenes," in *Proceedings of the IEEE/CVF International Conference on Computer Vision*, 2021, pp. 6029–6038. 2
- [39] Y. He, Y. Hu, W. Zhao, J. Li, Y.-J. Liu, Y. Han, and J. Wen, "Darkfeat: noise-robust feature detector and descriptor for extremely low-light raw images," in *Proceedings of the AAAI Conference on Artificial Intelligence*, vol. 37, no. 1, 2023, pp. 826–834. 2
- [40] E. McKinley and R. V. Allen, "Mariner jupiter/saturn 1977 navigation strategy," *Journal of Spacecraft and Rockets*, vol. 13, no. 8, pp. 494–501, 1976. 2
- [41] R. JACOBSON, S. SYNNOTT, and J. DIXON, "Navigation accuracy analysis for the mariner-jupiter-saturn 1977 mission," in *Astrodynamic Conference*, 1976, p. 833. 2
- [42] C. Kohlhaese and P. A. Penzo, "Voyager mission description," *Space science reviews*, vol. 21, no. 2, pp. 77–101, 1977. 2
- [43] M. M. Kuritsky, M. S. Goldstein, I. Greenwood, H. Lerman, J. McCarthy, T. Shanahan, M. Silver, and J. Simpson, "Inertial navigation," *Proceedings of the IEEE*, vol. 71, no. 10, pp. 1156–1176, 1983. 2
- [44] F. Touche and A. Price, *Wilderness navigation handbook*. Touche Publishing, 2004. 2
- [45] Y. Ding, J. Yang, V. Larsson, C. Olsson, and K. Åström, "Revisiting the p3p problem," in *Proceedings of the IEEE/CVF Conference on Computer Vision and Pattern Recognition*, 2023, pp. 4872–4880. 3, 9
- [46] T. Gao, M. Zhao, C. Xu, and H. Kong, "Night-rider: Nocturnal vision-aided localization in streetlight maps using invariant extended kalman filtering," in *2024 IEEE International Conference on Robotics and Automation (ICRA)*, 2024, pp. 10 238–10 244. 3, 4, 7, 9, 15
- [47] R. W. Wolcott and R. M. Eustice, "Visual localization within lidar maps for automated urban driving," in *2014 IEEE/RSJ International Conference on Intelligent Robots and Systems*. IEEE, 2014, pp. 176–183. 4
- [48] A. D. Stewart and P. Newman, "Laps-localisation using appearance of prior structure: 6-dof monocular camera localisation using prior pointclouds," in *2012 IEEE International Conference on Robotics and Automation*. IEEE, 2012, pp. 2625–2632. 4
- [49] G. Pascoe, W. Maddern, and P. Newman, "Direct visual localisation and calibration for road vehicles in changing city environments," in *Proceedings of the IEEE International Conference on Computer Vision Workshops*, 2015, pp. 9–16. 4
- [50] P. Neubert, S. Schubert, and P. Protzel, "Sampling-based methods for visual navigation in 3d maps by synthesizing depth images," in *2017 IEEE/RSJ International Conference on Intelligent Robots and Systems (IROS)*. IEEE, 2017, pp. 2492–2498. 4
- [51] X. Zuo, P. Geneva, Y. Yang, W. Ye, Y. Liu, and G. Huang, "Visual-inertial localization with prior lidar map constraints," *IEEE Robotics and Automation Letters*, vol. 4, no. 4, pp. 3394–3401, 2019. 4
- [52] X. Ding, Y. Wang, R. Xiong, D. Li, L. Tang, H. Yin, and L. Zhao, "Persistent stereo visual localization on cross-modal invariant map," *IEEE Transactions on Intelligent Transportation Systems*, vol. 21, no. 11, pp. 4646–4658, 2019. 4
- [53] T. Caselitz, B. Steder, M. Ruhnke, and W. Burgard, "Monocular camera localization in 3d lidar maps," in *2016 IEEE/RSJ International Conference on Intelligent Robots and Systems (IROS)*. IEEE, 2016, pp. 1926–1931. 4
- [54] C. Zhang, H. Zhao, C. Wang, X. Tang, and M. Yang, "Cross-modal monocular localization in prior lidar maps utilizing semantic consistency," in *2023 IEEE International Conference on Robotics and Automation (ICRA)*. IEEE, 2023, pp. 4004–4010. 4
- [55] X. Zuo, W. Ye, Y. Yang, R. Zheng, T. Vidal-Calleja, G. Huang, and Y. Liu, "Multimodal localization: Stereo over lidar map," *Journal of Field Robotics*, vol. 37, no. 6, pp. 1003–1026, 2020. 4
- [56] H. Yu, W. Zhen, W. Yang, J. Zhang, and S. Scherer, "Monocular camera localization in prior lidar maps with 2d-3d line correspondences," in *2020 IEEE/RSJ International Conference on Intelligent Robots and Systems (IROS)*. IEEE, 2020, pp. 4588–4594. 4, 13, 14
- [57] G. Zhou, H. Yuan, S. Zhu, Z. Huang, Y. Fan, X. Zhong, R. Du, and J. Gu, "Visual localization in a prior 3d lidar map combining points and lines," in *2021 IEEE International Conference on Robotics and Biomimetics (ROBIO)*. IEEE, 2021, pp. 1198–1203. 4
- [58] J. Leng, C. Sun, B. Wang, Y. Lan, Z. Huang, Q. Zhou, J. Liu, and J. Li, "Cross-modal lidar-visual-inertial localization in pre-built lidar point cloud map through direct projection," *IEEE Sensors Journal*, 2024. 4



- [59] J. Miao, K. Jiang, Y. Wang, T. Wen, Z. Xiao, Z. Fu, M. Yang, M. Liu, J. Huang, Z. Zhong *et al.*, “Poses as queries: End-to-end image-to-lidar map localization with transformers,” *IEEE Robotics and Automation Letters*, vol. 9, no. 1, pp. 803–810, 2023. 4
- [60] S. Shubodh, M. Omama, H. Zaidi, U. S. Parihar, and M. Krishna, “Lip-loc: Lidar image pretraining for cross-modal localization,” in *Proceedings of the IEEE/CVF Winter Conference on Applications of Computer Vision*, 2024, pp. 948–957. 4
- [61] Z. Zhao, H. Yu, C. Lyu, W. Yang, and S. Scherer, “Attention-enhanced cross-modal localization between spherical images and point clouds,” *IEEE Sensors Journal*, 2023. 4
- [62] P. Yin, L. Xu, J. Zhang, H. Choset, and S. Scherer, “i3dLoc: Image-to-range Cross-domain Localization Robust to Inconsistent Environmental Conditions,” in *Proceedings of Robotics: Science and Systems*, Virtual, July 2021. 4
- [63] D. Cattaneo, M. Vaghi, A. L. Ballardini, S. Fontana, D. G. Sorrenti, and W. Burgard, “Cmnet: Camera to lidar-map registration,” in *2019 IEEE Intelligent Transportation Systems Conference (ITSC)*, Oct 2019, pp. 1283–1289. 4, 13, 14
- [64] K. Chen, H. Yu, W. Yang, L. Yu, S. Scherer, and G.-S. Xia, “I2d-loc: Camera localization via image to lidar depth flow,” *ISPRS Journal of Photogrammetry and Remote Sensing*, vol. 194, pp. 209–221, 2022. 4
- [65] X. Wu, J. Xu, P. Hu, G. Wang, and H. Wang, “Lhmap-loc: Cross-modal monocular localization using lidar point cloud heat map,” in *2024 IEEE International Conference on Robotics and Automation (ICRA)*, 2024, pp. 8500–8506. 4, 13, 14
- [66] T. Qin, Y. Zheng, T. Chen, Y. Chen, and Q. Su, “A light-weight semantic map for visual localization towards autonomous driving,” in *2021 IEEE international conference on robotics and automation (ICRA)*. IEEE, 2021, pp. 11 248–11 254. 4
- [67] J.-H. Pauls, K. Petek, F. Poggenhans, and C. Stiller, “Monocular localization in hd maps by combining semantic segmentation and distance transform,” in *2020 IEEE/RSJ International Conference on Intelligent Robots and Systems (IROS)*. IEEE, 2020, pp. 4595–4601. 4
- [68] Z. Liao, J. Shi, X. Qi, X. Zhang, W. Wang, Y. He, X. Liu, and R. Wei, “Coarse-to-fine visual localization using semantic compact map,” in *2020 3rd International Conference on Control and Robots (ICCR)*. IEEE, 2020, pp. 30–37. 4
- [69] H. Wang, C. Xue, Y. Zhou, F. Wen, and H. Zhang, “Visual semantic localization based on hd map for autonomous vehicles in urban scenarios,” in *2021 IEEE International Conference on Robotics and Automation (ICRA)*. IEEE, 2021, pp. 11 255–11 261. 4
- [70] S. Leutenegger, S. Lynen, M. Bosse, R. Siegwart, and P. Furgale, “Keyframe-based visual-inertial odometry using nonlinear optimization,” *The International Journal of Robotics Research*, vol. 34, no. 3, pp. 314–334, 2015. 4
- [71] V. Usenko, N. Demmel, D. Schubert, J. Stückler, and D. Cremers, “Visual-inertial mapping with non-linear factor recovery,” *IEEE Robotics and Automation Letters*, vol. 5, no. 2, pp. 422–429, 2019. 4
- [72] A. I. Mourikis and S. I. Roumeliotis, “A multi-state constraint kalman filter for vision-aided inertial navigation,” in *Proceedings 2007 IEEE international conference on robotics and automation*. IEEE, 2007, pp. 3565–3572. 4
- [73] R. Gomez-Ojeda, Z. Zhang, J. Gonzalez-Jimenez, and D. Scaramuzza, “Learning-based image enhancement for visual odometry in challenging hdr environments,” in *2018 IEEE International Conference on Robotics and Automation (ICRA)*. IEEE, 2018, pp. 805–811. 4
- [74] E. Jung, N. Yang, and D. Cremers, “Multi-frame gan: Image enhancement for stereo visual odometry in low light,” in *Conference on Robot Learning*. PMLR, 2020, pp. 651–660. 4
- [75] H. Alismail, M. Kaess, B. Browning, and S. Lucey, “Direct visual odometry in low light using binary descriptors,” *IEEE Robotics and Automation Letters*, vol. 2, no. 2, pp. 444–451, 2016. 4
- [76] G. Pascoe, W. Maddern, M. Tanner, P. Piniés, and P. Newman, “Nid-slam: Robust monocular slam using normalised information distance,” in *Proceedings of the IEEE conference on computer vision and pattern recognition*, 2017, pp. 1435–1444. 4
- [77] P. Bergmann, R. Wang, and D. Cremers, “Online photometric calibration of auto exposure video for realtime visual odometry and slam,” *IEEE Robotics and Automation Letters*, vol. 3, no. 2, pp. 627–634, 2017. 4
- [78] A. Litvinov and Y. Y. Schechner, “Addressing radiometric nonidealities: A unified framework,” in *2005 IEEE Computer Society Conference on Computer Vision and Pattern Recognition (CVPR’05)*, vol. 2. IEEE, 2005, pp. 52–59. 4
- [79] H. Lu, H. Zhang, S. Yang, and Z. Zheng, “Camera parameters auto-adjusting technique for robust robot vision,” in *2010 IEEE International Conference on Robotics and Automation*. IEEE, 2010, pp. 1518–1523. 4
- [80] N. Weidner, S. Rahman, A. Q. Li, and I. Rekleitis, “Underwater cave mapping using stereo vision,” in *2017 IEEE International Conference on Robotics and Automation (ICRA)*. IEEE, 2017, pp. 5709–5715. 4
- [81] P. Nelson, W. Churchill, I. Posner, and P. Newman, “From dusk till dawn: Localisation at night using artificial light sources,” in *2015 IEEE International Conference on Robotics and Automation (ICRA)*. IEEE, 2015, pp. 5245–5252. 4
- [82] A. Barrau and S. Bonnabel, “The invariant extended kalman filter as a stable observer,” *IEEE Transactions on Automatic Control*, vol. 62, no. 4, pp. 1797–1812, 2016. 4, 5, 6
- [83] R. Hartley, M. Ghaafari, R. M. Eustice, and J. W. Grizzle, “Contact-aided invariant extended kalman filtering for robot state estimation,” *The International Journal of Robotics Research*, vol. 39, no. 4, pp. 402–430, 2020. 5
- [84] M. Brossard, S. Bonnabel, and A. Barrau, “Invariant kalman filtering for visual inertial slam,” in *2018 21st International Conference on Information Fusion (FUSION)*. IEEE, 2018, pp. 2021–2028. 5, 10
- [85] Y. Song, Z. Zhang, J. Wu, Y. Wang, L. Zhao, and S. Huang, “A right invariant extended kalman filter for object based slam,” *IEEE Robotics and Automation Letters*, vol. 7, no. 2, pp. 1316–1323, 2021. 5
- [86] Y. Yang, B. P. W. Babu, C. Chen, G. Huang, and L. Ren, “Analytic combined imu integration (aci 2) for visual inertial navigation,” in *2020 IEEE International Conference on Robotics and Automation (ICRA)*. IEEE, 2020, pp. 4680–4686. 5, 6
- [87] E. R. Potokar, K. Norman, and J. G. Mangelson, “Invariant extended kalman filtering for underwater navigation,” *IEEE Robotics and Automation Letters*, vol. 6, no. 3, pp. 5792–5799, 2021. 5
- [88] Y. Yang, C. Chen, W. Lee, and G. Huang, “Decoupled right invariant error states for consistent visual-inertial navigation,” *IEEE Robotics and Automation Letters*, vol. 7, no. 2, pp. 1627–1634, 2022. 6, 10
- [89] C.-Y. Wang, A. Bochkovskiy, and H.-Y. M. Liao, “Yolov7: Trainable bag-of-freebies sets new state-of-the-art for real-time object detectors,” in *Proceedings of the IEEE/CVF conference on computer vision and pattern recognition*, 2023, pp. 7464–7475. 7, 14
- [90] W. Xu, Y. Cai, D. He, J. Lin, and F. Zhang, “Fast-lid2: Fast direct lidar-inertial odometry,” *IEEE Transactions on Robotics*, vol. 38, no. 4, pp. 2053–2073, 2022. 7
- [91] Y. Wang, Z. Sun, C.-Z. Xu, S. E. Sarma, J. Yang, and H. Kong, “Lidar iris for loop-closure detection,” in *2020 IEEE/RSJ International Conference on Intelligent Robots and Systems (IROS)*. IEEE, 2020, pp. 5769–5775. 7
- [92] F. Dellaert, “Factor graphs and gtsam: A hands-on introduction,” *Georgia Institute of Technology, Tech. Rep.*, vol. 2, p. 4, 2012. 7
- [93] G. Zhang, J. H. Lee, J. Lim, and I. H. Suh, “Building a 3-d line-based map using stereo slam,” *IEEE Transactions on Robotics*, vol. 31, no. 6, pp. 1364–1377, 2015. 7
- [94] T. D. Barfoot, *State estimation for robotics*. Cambridge University Press, 2024. 7
- [95] H. W. Kuhn, “The hungarian method for the assignment problem,” *Naval research logistics quarterly*, vol. 2, no. 1-2, pp. 83–97, 1955. 8, 9
- [96] S. Suzuki *et al.*, “Topological structural analysis of digitized binary images by border following,” *Computer vision, graphics, and image processing*, vol. 30, no. 1, pp. 32–46, 1985. 8
- [97] Z. Zhang, Y. Song, S. Huang, R. Xiong, and Y. Wang, “Toward consistent and efficient map-based visual-inertial localization: Theory framework and filter design,” *IEEE Transactions on Robotics*, 2023. 10
- [98] K. Wu, T. Zhang, D. Su, S. Huang, and G. Dissanayake, “An invariant-ekf vins algorithm for improving consistency,” in *2017 IEEE/RSJ international conference on intelligent robots and systems (IROS)*. IEEE, 2017, pp. 1578–1585. 10
- [99] M. Li and A. I. Mourikis, “High-precision, consistent ekf-based visual-inertial odometry,” *The International Journal of Robotics Research*, vol. 32, no. 6, pp. 690–711, 2013. 10
- [100] T.-M. Nguyen, S. Yuan, T. H. Nguyen, P. Yin, H. Cao, L. Xie, M. Wozniak, P. Jensfelt, M. Thiel, J. Ziegenbein *et al.*, “Mcd: Diverse large-scale multi-campus dataset for robot perception,” in *Proceedings of the IEEE/CVF Conference on Computer Vision and Pattern Recognition*, 2024, pp. 22 304–22 313. 12, 13